Frictional behavior of oceanic transform faults and its influence on earthquake characteristics

Yajing Liu,[1,2] Jeffrey J. McGuire,[2] and Mark D. Behn[2]

Received 13 November 2011; revised 6 March 2012; accepted 8 March 2012; published 26 April 2012.

[1] We use a three-dimensional strike-slip fault model in the framework of rate and state-dependent friction to investigate earthquake behavior and scaling relations on oceanic transform faults (OTFs). Gabbro friction data under hydrothermal conditions are mapped onto OTFs using temperatures from (1) a half-space cooling model, and (2) a thermal model that incorporates a visco-plastic rheology, non-Newtonian viscous flow and the effects of shear heating and hydrothermal circulation. Without introducing small-scale frictional heterogeneities on the fault, our model predicts that an OTF segment can transition between seismic and aseismic slip over many earthquake cycles, consistent with the multimode hypothesis for OTF ruptures. The average seismic coupling coefficient χ is strongly dependent on the ratio of seismogenic zone width W to earthquake nucleation size h^*; χ increases by four orders of magnitude as W/h^* increases from ~1 to 2. Specifically, the average $\chi = 0.15 \pm 0.05$ derived from global OTF earthquake catalogs can be reached at $W/h^* \approx 1.2$–1.7. Further, in all simulations the area of the largest earthquake rupture is less than the total seismogenic area and we predict a deficiency of large earthquakes on long transforms, which is also consistent with observations. To match these observations over this narrow range of W/h^* requires an increase in the characteristic slip distance d_c as the seismogenic zone becomes wider and normal stress is higher on long transforms. Earthquake magnitude and distribution on the Gofar and Romanche transforms are better predicted by simulations using the visco-plastic model than the half-space cooling model.

Citation: Liu, Y., J. J. McGuire, and M. D. Behn (2012), Frictional behavior of oceanic transform faults and its influence on earthquake characteristics, *J. Geophys. Res.*, *117*, B04315, doi:10.1029/2011JB009025.

1. Introduction

[2] Oceanic transform faults (OTFs), which separate individual spreading segments along the global mid-ocean ridge system, are primarily characterized by strike-slip motion. In contrast to continental strike-slip faults, a large percentage of slip on OTFs, on average ~85%, occurs in the form of aseismic creep [*Boettcher and Jordan*, 2004]. The largest OTF earthquakes are small (moment magnitude 6 to 7) even though some faults are over 1000 km long, indicating that such earthquakes ruptured only a small portion of the total fault area. The focal depths of OTF earthquakes appear to be bounded by an isotherm near 600°C, based on ocean bottom seismometer (OBS) deployments [*Wilcock et al.*, 1990], teleseismic waveform modeling and earthquake slip inversions [*Abercrombie and Ekström*, 2001; *Braunmiller and Nábělek*, 2008]. To date, studies to understand OTF earthquake rupture processes and seismic cycles have focused on statistical analysis of earthquake catalogs [*Bird et al.*, 2002; *Bohnenstiehl et al.*, 2002; *Boettcher and Jordan*, 2004; *McGuire et al.*, 2005; *Boettcher and McGuire*, 2009; *Kagan et al.*, 2010] and source inversion of large events [*Abercrombie and Ekström*, 2001; *Braunmiller and Nábělek*, 2008; *McGuire*, 2008; *Sykes and Ekström*, 2012]. These efforts have been limited because global catalogs span multiple earthquake cycles on only the fastest slipping faults, and global seismic networks are far removed from almost all OTFs. More recently, experiments utilizing high-quality OBS data to resolve the rupture process during OTF earthquakes have begun to provide an improved level of detail that can be compared with modeling studies [*McGuire et al.*, 2012].

[3] Despite the limited data available, several robust scaling relations have been established for OTF earthquake source processes. Specifically, *Boettcher and Jordan* [2004] used earthquake catalog data from a global compilation of 65 OTFs with a combined length of 16,410 km to define two characteristic scaling relations. (1) The effective seismic area A_E, the total area on the fault that ruptures seismically averaged over many earthquake cycles, scales linearly with the total thermal area A_T above the 600°C isotherm as determined by a half-space cooling model. As shown in Figure 1a, the maximum likelihood value of the coupling coefficient $\chi \equiv A_E/A_T$ is roughly a constant of 0.15 ± 0.05, independent of full ridge spreading rate V_{pl} or transform length L. (2) The rupture area of the largest earthquake recorded on an OTF, A_c (also called upper cutoff area), does not scale directly with

[1]Department of Earth and Planetary Sciences, McGill University, Montreal, Quebec, Canada.
[2]Department of Geology and Geophysics, Woods Hole Oceanographic Institution, Woods Hole, Massachusetts, USA.

0148-0227/12/2011JB009025

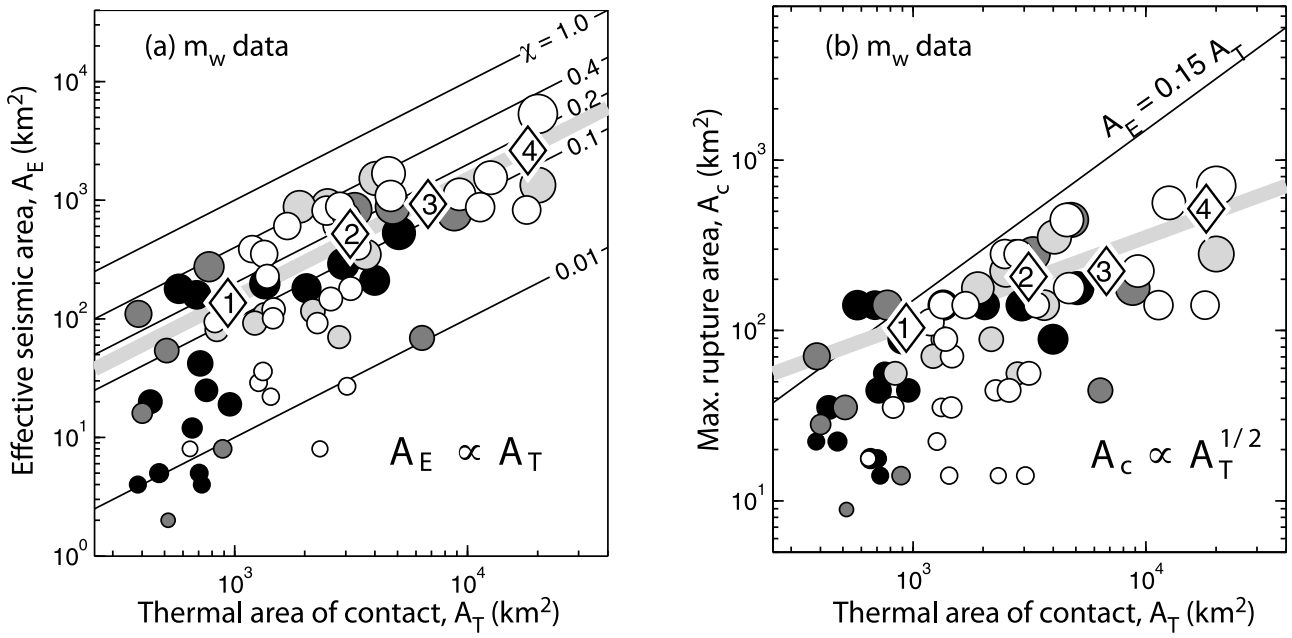

Figure 1. (a) Effective seismic area A_E versus thermal area A_T from the Global GMT catalog of OTF earthquakes, 1976-2002. Circles show data for earthquake on individual OTFs; circle size is proportional to the cumulative moment on each OTF and shade is based on slip rate V_{pl} (darker color for higher V_{pl}). The numbered diamonds show the maximum likelihood estimates of A_E for A_T in four bins: [350:2000] km^2, [2000:4500] km^2, [4500:10000] km^2, and greater than 10000 km^2. (b) Rupture area of largest earthquake A_c versus A_T. Calculations for A_c assume a constant stress drop of $\Delta\sigma$ = 3 MPa and total displacement in the form $(\Delta\sigma/\mu)\sqrt{L_c W_c}$, where L_c and W_c are the rupture length and width, μ is shear modulus [modified from *Boettcher and Jordan*, 2004].

the thermal area A_T. Rather, *Boettcher and Jordan* [2004] found $A_c \propto A_T^{0.5}$ over two orders of magnitude (Figure 1b). Recently compiled OTF earthquakes from 2002–2009 GCMT catalog correspond very well with the frequency-moment distribution predicted using these two scaling relations [*Boettcher and McGuire*, 2009]. By contrast, the assumption that the largest earthquake would rupture the entire transform fault, i.e., $A_c = A_T$, cannot explain the observed frequency-magnitude distribution, using either a partial (0.15) or full (1.0) coupling coefficient.

[4] Two hypotheses that have been proposed to explain the above scaling relations involve "single-mode" or "multi-mode" slip on an OTF. In the single-mode model, seismic rupture persistently occurs on a fully coupled A_c-sized patch ($A_c \ll A_T$) over many earthquake cycles, while the rest of the fault always slips aseismically. The difference between A_T and A_c would then have to be explained by spatial variations in frictional stability properties. For example, the presence of hydrated ultramafic minerals of the serpentine group on OTFs [*Tucholke and Lin*, 1994; *Cannat et al.*, 1995] may promote aseismic slip at slow plate tectonics speeds [*Reinen et al.*, 1994]. Moreover, a single fault may have more than one persistently fully coupled patch, as has been observed on the Blanco Ridge, west Gofar and Eltanin transform fault segments [*McGuire*, 2008; *Sykes and Ekström*, 2012]. In the multimode model, slip can occur seismically or aseismically over the entire thermal area A_T. A possible scenario involves frictional properties that evolve temporally between unstable and stable sliding on fault patches, as inferred from laboratory experiments on serpentinite gouge [*Reinen*, 2000a, 2000b].

[5] In this paper, we study oceanic transform fault earthquake behavior and the associated scaling relations from a new perspective: applying a lab-derived rate and state-dependent friction law to model earthquake cycles and construct earthquake catalogs on OTFs. The frictional parameter $a-b$ is adapted from the experimental measurements on gabbro gouge under hydrothermal conditions, and mapped to distributions on the OTFs using temperatures calculated from (1) a half-space cooling model, and (2) a thermal model that takes in account additional physical processes such as visco-plastic behavior in the lithosphere, non-Newtonian temperature-dependent viscous flow in the underlying mantle, and the effects of shear heating and hydrothermal circulation [*Roland et al.*, 2010].

[6] Without involving small-scale heterogeneities such as along-strike variations in frictional stability, we show that the low seismic coupling and deficiency of large earthquakes observed on global OTFs can be explained if the seismogenic zone width (W) is on the order of (~1.2 to 1.7 times) the earthquake nucleation size (h^*). This is consistent with previous studies that show the ratio of the two characteristic lengths is a key parameter that controls the transition from aseismic to seismic slip in the context of episodic slow slip events [*Liu and Rice*, 2007; *Rubin*, 2008] and scaling of small repeating earthquakes [*Chen and Lapusta*, 2009]. Of course a model with spatially variable friction properties could be tuned to replicate both of the scaling relations. More complicated physical mechanisms such as dilatancy could also be incorporated to prevent full-fault ruptures. However, the goal of this study is to investigate if the simplest, uniform

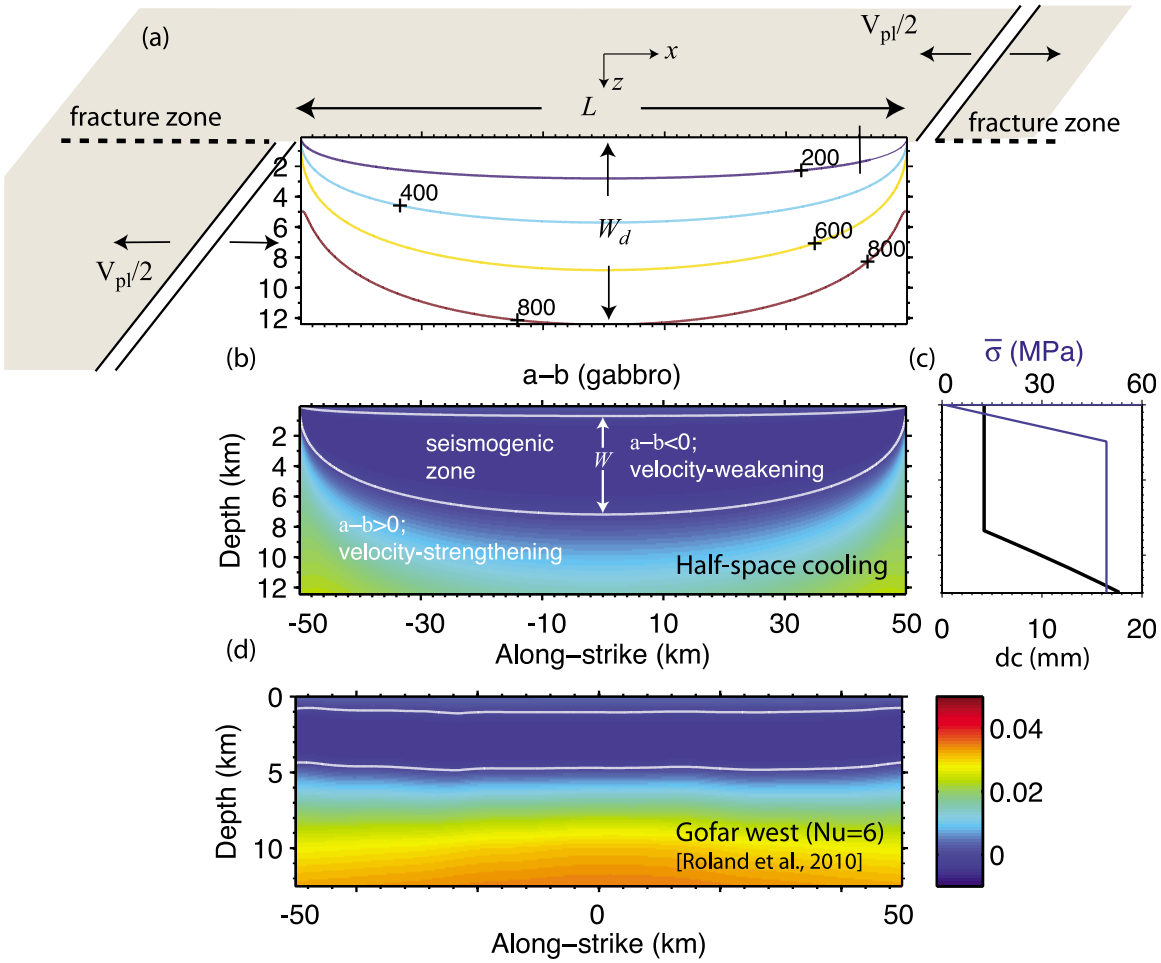

Figure 2. Model geometry of an OTF embedded in an elastic half-space. Illustrated is a case for an EPR Gofar-like short (L = 100 km) fast-slipping (V_{pl} = 140 mm/yr) transform. (a) Temperature isotherms (colored lines) calculated from a half-space cooling model, with thermal diffusivity $\kappa = 5$ mm^2/s. (b) Distribution of friction parameter $a-b$ on the fault, mapped from gabbro data [*He et al.*, 2007] using thermal profile in Figure 2a. Upper white line shows the velocity-strengthening (VS) to velocity-weakening (VW) transition, and the lower white line shows VW to VS transition. A_T is defined as the VW area (seismogenic) zone between the two white lines. (c) Typical distributions of effective normal stress (blue) and characteristic slip distance (black) with depth. (d) Friction parameter $a-b$ on the fault mapped using west Gofar thermal structure calculated using the visco-plastic model with Nusselt number $N_u = 6$ [*Roland et al.*, 2010]. Solid white lines delineate the transition from VS to VW (upper line) and VW to VS (lower line). Seismogenic zone is the area between these two lines.

frictional model can reproduce the scaling relations without resorting to arbitrary heterogeneity tuning.

2. Modeling Procedures

2.1. Geometry

[7] The framework of a 3-D strike-slip model with rate and state-dependent friction was first introduced by *Rice* [1993] and later analyzed with simplified mirror symmetry boundary conditions at the Earth's surface by *Rice and Ben-Zion* [1996]. Here, we modified the 3-D model used by *Liu and Rice* [2005] for calculating seismic and aseismic slip sequences on subduction megathrusts, to a strike-slip fault model, including the free surface effect, to simulate slip on an oceanic transform fault over many earthquake cycles. We use a vertical planar frictional interface, defined by the x-z plane in the Cartesian coordinate system (x is along-strike direction; z is vertical), to simulate the transform fault in a ridge-transform-ridge system (Figure 2). The planar fault offsets two ridge spreading segments by a distance L, and is loaded by the half spreading rate $V_{pl}/2$ on each side of the fault (total relative displacement rate of V_{pl}). The adjacent fracture zones are modeled as extensions of the OTF with the same loading rate V_{pl} and a time-constant slip rate $V = V_{pl}$ such that effectively slip on the fracture zones do not contribute to the stress evolution on the OTF. Ideally, the fracture zones in the model would extend infinitely along the OTF strike, however, this would be extremely computationally expensive. Therefore, to choose an appropriate fracture zone length L_{fz}, we compared model results using (1) $L_{fz} = L/2$, and (2) $L_{fz} = 3L/2$ for several sets of simulations. The entire along-strike domain length, $2L$ and $4L$, respectively, is repeated periodically such

that Fast Fourier Transform can be applied to reduce the computation time by a factor of $(\log_2 N_l)/N_l$, where N_l is the number of grids along the strike and is chosen to be a power of 2. The modeled slip history, including maximum slip velocity, cumulative slip at several depths and spatial earthquake rupture patterns, is almost identical with the two choices of L_{fz}. An even longer fracture zone is expected to produce very similar results. Thus, in the simulations presented below, a fracture zone of length $L_{fz} = L/2$ is applied on each side of the OTF. The present model neglects the coupling effect from any neighboring OTFs.

[8] Fault slip $\delta(x, z, t)$ is calculated for the portion of the fault $-L/2 < x < L/2$ and $0 < z < W_d$ (W_d = 12.5 km in Figure 2, and may be different in other configurations, e.g., deeper for colder, slower slipping faults). A uniform motion at the long-term spreading rate V_{pl} is imposed at $W_d < z < +\infty$, below the depths of seismicity and postseismic transients. In the present model, we only consider slip in the strike direction, i.e., no dip component.

2.2. Elastic Relation Between Stress and Slip

[9] We model the contribution of slip on the fault to the shear stress distribution according to the following "quasi-dynamic" relation [*Rice*, 1993]:

$$\tau(x,z,t) = -\int_{-L/2}^{L/2}\int_{0}^{W_d} k(x-x',z,z')\left[\delta(x',z',t) - V_{pl}t\right]dx'dz' - \eta\frac{\partial\delta(x,z,t)}{\partial t}. \quad (1)$$

The highly singular stiffness kernel $k(x - x', z, z')$ is calculated here, in discretized form, as the set of shear stresses on a grid centered at (x, z) from the quasi-static solution for a uniform slip over a dislocation on a grid centered at (x', z') in an elastic half-space [*Okada*, 1992]. A radiation damping factor η is included to prevent the slip velocity from becoming unbounded during instabilities [*Rice*, 1993]. The choice of $\eta = \mu/(2c_s)$ (μ is shear modulus and c_s is shear wave speed) allows equation (1) to exactly incorporate the elastodynamic result for how instantaneous changes in τ and δ are related to each other. Equation (1) is thus dynamically correct in its instantaneous response, and in producing a long-term static response between stress and slip. It does not incorporate the wave-mediated transitions between those states. In 2-D and 3-D strike slip models [*Lapusta et al.*, 2000; *Lapusta and Rice*, 2003; *Lapusta and Liu*, 2009], this "quasi-dynamic" approximation produces similar earthquake sequences as predicted from fully elastodynamic modeling, but with moderately less coseismic slip, slower slip velocity and rupture speeds in earthquake events. However, over many earthquake cycles, the ratios of cumulative seismic moment and total moment appear to be comparable with the two approaches [*Lapusta and Rice*, 2003]. In this study, we use the "quasi-dynamic" approximation so that extensive simulation cases can be conducted within the broad parameter space that includes different OTF configurations, thermal profiles and frictional properties.

2.3. Friction Law

[10] We use a single-state-variable form of the laboratory-derived rate and state-dependent friction law, in which the friction coefficient f is a function of the sliding velocity V and the state variable θ. Under steady state conditions, θ can be interpreted as the average contact time of asperities on the sliding interface [*Dieterich*, 1979; *Ruina*, 1983]. In particular, the frictional resistance can be expressed as

$$\tau = \bar{\sigma}f = \bar{\sigma}[f_0 + a\ln(V/V_0) + b\ln(V_0\theta/d_c)], \quad (2)$$

where the effective normal stress $\bar{\sigma} = \sigma - p$ is defined as the difference between the normal stress σ and the pore pressure p on the fault. The rate and state friction parameters a and $a-b$ can be interpreted, respectively, as the instantaneous change in f and the change in the steady state friction f_{ss} in response to a step change in velocity: $a = V(\partial f/\partial V)_{inst}$, $a - b = V(df_{ss}/dV)$. d_c is the characteristic slip distance over which state θ evolves after a velocity step. V_0 is a reference velocity, taken to be 10^{-6} m/s in the calculations, and f_0 is a nominal friction coefficient when $V = V_0$ at steady state. Near $V = 0$, we use a regularized form of the friction law

$$\tau = a\bar{\sigma}\,\mathrm{arcsinh}\left[\frac{V}{2V_0}\exp\left(\frac{f_0 + b\ln(V_0\theta/d_c)}{a}\right)\right], \quad (3)$$

as justified by a thermally activated description of slip at asperity contacts [*Rice and Ben-Zion*, 1996; *Lapusta et al.*, 2000; *Rice et al.*, 2001]. In this study, we use the "ageing" version of state evolution law, which allows friction to evolve on stationary contacts as observed in the lab [*Beeler et al.*, 1994],

$$\frac{d\theta}{dt} = 1 - \frac{V\theta}{d_c}. \quad (4)$$

Compared to the other commonly used version of state evolution "slip" law, the "ageing" law requires less numerical resolution, allowing us to extensively explore the large parameter space in this study. The steady state friction $f_{ss} = f_0 + (a - b)\ln(V/V_0)$, when $\theta = \theta_{ss} = d_c/V$, is the same for both the "ageing" and "slip" laws.

[11] The rate and state friction exhibits steady state velocity-strengthening (stable sliding) if $a - b > 0$, and steady state velocity-weakening (potentially unstable sliding) if $a - b < 0$. Instabilities (e.g., earthquakes) can only develop when the velocity-weakening region of the fault is greater than a critical nucleation size; theoretical estimates of the earthquake nucleation size h^* for 2-D problems are derived by *Rice and Ruina* [1983] and *Rubin and Ampuero* [2005]. For the geometry $L \gg W_d$ of modeled OTFs, we define the nucleation size as

$$h^* = h^*_{RA} = \frac{2}{\pi}\frac{\mu^* b d_c}{(b-a)^2\bar{\sigma}}, \quad (5)$$

where h^*_{RA} is the 2-D estimate of h^* by *Rubin and Ampuero* [2005] from energy balance of a quasi-statically expanding crack when $a/b > 0.5$. Effective shear modulus $\mu^* = \mu$ for mode III and $\mu^* = \mu/(1 - \nu)$ for mode II cracks.

2.4. Frictional Parameters

[12] Friction experiment data for gabbro gouge under hydrothermal conditions were recently reported by *He et al.* [2007]. Although the gabbro data are limited, compared to the comprehensive studies conducted on granite, and are highly scattered at some temperature ranges, we make tentative use

of them in our OTF earthquake models as the first friction data set available for the oceanic lithosphere. The major distinctive features of the temperature-dependent $a-b$ gabbro data are: (1) the velocity-weakening to strengthening transition occurs around 500°C under supercritical water conditions, compared to at ~350°C for wet granite [*Blanpied et al.*, 1998], and (2) $a-b$ remains less than 0.01 at higher temperatures up to ~600°C, about one order of magnitude smaller than that of wet granite at comparable conditions. We approximate the temperature-dependent $a-b$ data, as shown by *He et al.* [2007, Figure 3] and *Liu and Rice* [2009, Figure 2], by linear segments that cover different stability regimes, specifically with ends at $(T, a-b) = (0, 0.0035)$, $(100, -0.0035)$, $(416, -0.0035)$, $(520, 0.001)$, where temperature T is in °C. Linear extension is assumed for temperatures higher than 520°C. The parameter $a-b$ are then mapped onto the fault using a thermal model as described in section 2.5.

[13] The normal stress is assumed to follow a typical overburden stress gradient $\sigma = (28\ \text{MPa/km}) \times z$, and the pore pressure is given by either the hydrostatic gradient $p = (10\ \text{MPa/km}) \times z$ or by $p = \max(\text{hydrostatic}, \sigma - \bar{\sigma}_{const})$, where $\bar{\sigma}_{const}$ is a constant value of $\bar{\sigma}$ at depth. The latter incorporates the elevated pore pressure concepts of *Rice* [1992]. Such an assumption could be appropriate for an oceanic transform fault with seawater permeating to greater depths. As a result, the effective normal stress $\bar{\sigma}$ increases with depth at a gradient of 18 MPa/km until it reaches $\bar{\sigma}_{const}$, which we choose to be 50 MPa in all cases. As will be shown in section 3, the choice of 50 MPa, together with other parameters (e.g., d_c), can predict earthquakes of magnitudes and recurrence intervals reasonably close to those observed on short, fast-slipping OTFs such as Gofar [*McGuire*, 2008]. Mechanical models for oceanic transform faults also predict that shear stress on OTFs, hence normal stress given a constant friction coefficient, is low, in order to explain the observed patterns of faulting and seismicity near a ridge-transform intersection [*Behn et al.*, 2002].

[14] As in other numerical simulations of this type [e.g., *Liu and Rice*, 2005; *Lapusta and Liu*, 2009], in order to properly resolve the fault and the bordering fracture zones as long as 1000 km and to make simulations computationally tractable it is necessary to take d_c in the range of mm, which is much larger than typical experimental values (~5 to 100 μm) measured at slow loading velocities. An example of the d_c distribution along the fault is shown in Figure 2c, where $d_c = 4.2$ mm within the seismogenic zone is followed by a linear increase up to ~17 mm at the down-dip end of the fault. Larger values of d_c are used for longer OTFs; d_c is in the range of ~10 to 20 mm in the seismogenic zone and up to 50 to 100 mm at the down-dip end of the fault for the $L =$ 500 km cases. The possible reasons and implications of larger d_c on longer faults will be discussed in section 4. As will be shown in section 3, our modeled earthquake scaling relations are dependent on the length ratio W/h^*, where W is the seismogenic zone width. Thus, by equation (5), if a smaller d_c was used and W, friction parameters a and b are kept unchanged in the simulations, a proportionally smaller effective normal stress $\bar{\sigma}$ would result in the same scaling relations. However, the modeled earthquake magnitudes, recurrence intervals and stress drops would also become smaller. Using the typical parameters as described above, for the longest modeled OTF ($L = 500$ km) we can resolve the cohesive zone in a rupture process (the intermediate transitional region between broken and unbroken material) $\Lambda_0 = C_0 \mu d_c / (b\bar{\sigma})$, where C_0 is a constant of order unity, by $3.2h$ (h is the grid size) for a representative $W/h^* = 1.44$ case. This satisfies the numerical resolution criterion that Λ_0 must be at least of the size of h for 3-D quasi-dynamic simulations [*Lapusta and Liu*, 2009].

[15] In order to satisfy the higher resolution required for larger W/h^* (smaller d_c) and keep the calculation within our computational limit, we used a smaller $a = 0.01$ for a few $L =$ 100 km cases with W/h^* near or greater than 2 and for some cases with the longest $L = 500$ km. With $a - b = -0.0035$ kept constant at most the seismogenic depth, this is equivalent to have a smaller b value and thus a larger cohesive zone Λ_0 that allows coarser resolutions. Calculations were also performed using both $a = 0.01$ and $a = 0.015$ in the same W/h^* range. The resulted seismic coupling coefficient χ and largest earthquake rupture area A_c are highly comparable with the two parameter a choices, suggesting that a small variation in a, at least in the vicinity of 0.015, does not affect the general trends and scaling relations we later present in Figures 8 and 9.

[16] Small along-strike perturbations are introduced to parameters a and $a-b$ in order to perturb the system from its initial near steady state into a nonuniform slip mode. Starting with these parameters defined by the fault thermal structure (section 2.5, Figure 2b), the parameter values were reduced by 2% in along-strike segment $[-L/2, -L/4]$, 3% in $[-L/4, 0]$, unaltered in $[0, L/4]$ and 3% in $[L/4, L/2]$. We note that in our simulations there is no obvious correlation between the earthquakes and the segments where the small nonuniformities were introduced; significantly larger perturbations do induce such a correlation. Simulations started from different nonuniform initial conditions (perturbed from steady state) also result in similar heterogeneous slip histories [*Liu and Rice*, 2005].

2.5. Transform Fault Thermal Structure

[17] A commonly used estimate for oceanic transform fault thermal structure is the average of temperatures predicted from a half-space cooling model on either side of the fault [e.g., *McKenzie*, 1969; *Engeln et al.*, 1986]:

$$\frac{T - T_0}{T_m - T_0} = erf\left[\frac{z}{2\sqrt{2\kappa(x + L/2)/V_{pl}}}\right], \tag{6}$$

where $T_0 = 0$°C and $T_m = 1300$°C are temperatures assumed of the seafloor surface and the mantle, respectively; κ is thermal diffusivity, assumed to be a constant; and x, z are as defined in Figure 2a. An example of the half-space cooling temperature profile is shown in Figure 2a, for a short/fast spreading OTF ($L = 100$ km, $V_{pl} = 140$ mm/yr, $\kappa = 5$ mm^2/s). The classic half-space cooling model produces results that can successfully predict the maximum depth of transform earthquakes [*Engeln et al.*, 1986; *Abercrombie and Ekström*, 2001; *Braunmiller and Nábělek*, 2008] and can be used to estimate seismic coupling along oceanic transform faults [*Bird et al.*, 2002; *Boettcher and Jordan*, 2004]. However,

Table 1. Parameters Constant for All Simulations

Parameter	Symbol	Value
Shear modulus	μ	30 GPa
Shear wave speed	c_s	3 km/s
Poisson's ratio	ν	0.25
Reference velocity	V_0	1 μm/s
Steady state friction coefficient at V_0	f_0	0.6
Effective normal stress	$\bar{\sigma}_{const}$	50 MPa
Seafloor seawater temperature	T_0	0°C
Mantle temperature	T_m	1300°C

it neglects many physical processes that occur in the oceanic crust and upper mantle. To address these limitations, *Behn et al.* [2007] and *Roland et al.* [2010] investigated the importance of fault rheology on the thermomechanical behavior of transforms. Their models incorporated a visco-plastic rheology to simulate brittle failure in the lithosphere and a non-Newtonian temperature-dependent viscous flow in the underlying mantle, as well as effects of shear heating and hydrothermal circulation on the resulting temperature structure. The inclusion of the brittle rheology directly contributes to a warmer thermal structure which is consistent with the geologic and geophysical observations from ridge-transform environments [*Behn et al.*, 2007]. The resulting thermal structure produces a similar seismogenic area to that predicted by a half-space cooling model, but in contrast to the half-space model, the depth of the 600°C isotherm and the width of the seismogenic zone are nearly constant along the fault. *Roland et al.* [2010] modeled the efficiency of hydrothermal circulation using a Nusselt number (N_u) approach [e.g., *Sleep*, 1975; *Phipps Morgan et al.*, 1987], in which the thermal conductivity is increased by a constant factor, N_u, over the background conductivity for intact rocks. N_u is thus the ratio of the total heat transported within a permeable layer to heat transferred by conduction alone. The depth of the isotherms increases with N_u, but the area between the ~350 and 600°C isotherms remains relatively constant for values of N_u up to ~12.

[18] In this study, we use temperatures predicted from both the half-space cooling model and the visco-plastic model of *Roland et al.* [2010] to map the gabbro frictional parameters onto the fault plane. As shown in Figure 2, the shape of the seismogenic zone, defined as the area of velocity-weakening, generally follows that of the isotherms. For the half-space cooling model, the maximum seismogenic zone width $W_{\max} \sim 6.6$ km is reached at the along-strike center $x = 0$ (Figure 2b). For a visco-plastic thermal structure with $N_u = 6$ for the west segment of Gofar, the width of the seismogenic zone is relatively uniform along the strike (Figure 2d). As will be discussed in section 3, the ratio of $W_{\max}$ to the earthquake nucleation size h^* is a key parameter controlling the seismic coupling on the modeled OTFs. The predictions of both thermal models will be compared for specific fault geometries and the results will be discussed in the context of the observed OTF scaling relations.

[19] Table 1 lists the values of parameters that are constant in all simulation cases. Table 2 lists the OTF parameters used in each simulation case that are shown in Figure 8. As discussed above, the parameters are chosen, wherever possible, to match measurements from appropriate laboratory experiments, or for consistency with seismicity studies or inferences from theory, although some are constrained by considerations of computational tractability.

3. Numerical Results and Comparison to Observations

[20] In this section we first present the earthquake sequence modeling results for two end-member OTF scenarios. The first scenario is for a short transform fault associated with a fast spreading ridge, such as the Gofar, Discovery, Quebrada system along East Pacific Rise. For this scenario, we choose L = 100 km and V_{pl} = 140 mm/yr as

Table 2. OTF Parameters for All Simulation Cases Shown in Figure 8[a]

OTF Length L (km)	Depth W_d (km)	Plate Rate V_{pl} (mm/yr)	Thermal Model, κ (mm^2/s), or N_u	W/h^*	a	Figure Number
100	12.5	140	H-S, 5	0.91	0.015	
				1.01		
				1.16		4a
				1.26		4b
				1.36		
				1.48		
				1.63		3, 4c, 10c
				2.02		4d
				2.71		
			H-S, 8	3.45		
			H-S, 5	2.12	0.01	
				2.64		
100	12.5	140	V-P, 6	1.18	0.015	
				1.36		
				1.58		5, 10d
				1.90		
				2.37		
				2.05	0.01	
				2.47		
				3.08		6
150	18.75	140	H-S, 5	1.33	0.015	
				1.48		
				1.65		
200	18.75	140	H-S, 5	1.43	0.015	
300	28.125	30	H-S, 2	1.38		
				1.58	0.015	
500	31.25	30	H-S, 1	0.99	0.015	
				1.16		
				1.38		
				1.73		7, 10f
				1.11	0.01	
				1.28		
				1.51		
				1.80		
				2.25		
				2.96		
500	23.4375	30	V-P, 8	1.18	0.01	
				1.48		
				1.52		
				1.58		10g
				1.63		
				1.70		
				1.75		
				1.83		
				1.97		
				2.37		
				2.96		

[a]The corresponding figure number, if the individual case is shown, is also listed. Blank means value is the same as in the previous case (except figure numbers). Thermal diffusivity κ in mm^2/s is given if a half-space cooling (H-S) thermal model is used. Nusselt number N_u is given if a visco-plastic (V-P) thermal model is used.

shown in Figure 2. Section 3.1.1 presents results using fault temperatures that are calculated from the half-space cooling model. A special case for the Gofar transform, where visco-plastic thermal structure and constraints from OBS deployments are available, is presented in section 3.1.2. The second end-member scenario is for a long transform fault (L = 500 km) associated with a slow spreading ridge (V_{pl} = 30 mm/yr), such as the Romanche and Doldrums along Mid-Atlantic Ridge. Both half-space cooling and visco-plastic thermal models are used for this group of calculations. We do not show the half-space cooling temperature profile or the resulting $a-b$ distribution for the long/slow OTF scenario, as they are similar in shape to those in Figure 2, except with larger fault dimensions. In addition, we also conduct simulations for several intermediate configurations, to check whether their results fall in the range defined by the two end-member scenarios. Comparisons of modeled earthquake scaling relations as well as earthquake magnitude and distribution to OTF observations are presented later in this section.

3.1. Short, Fast Slipping Transform Fault

3.1.1. Half-Space Cooling Thermal Model

[21] Using a half-space cooling model with diffusivity κ = 5 mm^2/s and the simplified gabbro friction data as described above, the resulted $a-b$ distribution is shown in Figure 2b. Parameter a is held constant at 0.015 except where $a = a - b$ ($b = 0$) in the deep velocity-strengthening region. In the OTF case shown in Figure 3, we assume d_c = 7 mm and $\bar{\sigma}$ = 50 MPa, which combined with a and b results in an earthquake nucleation size h^* = 4.05 km (equation (5)). The maximum seismogenic zone width $W_{\max}$ is about 6.6 km, resulting in $W_{\max}/h^* \approx 1.63$.

[22] Figure 3 summarizes the simulation results for the short, fast slipping transform over a 50 year time period. A general characteristic of the slip pattern is that seismic and slow slip events occur roughly every 2–4 years. Here, "seismic" is defined when the maximum slip velocity on the fault $V_{\max}$ exceeds a threshold V_{seis} = 5 mm/s; "slow slip" is defined when $V_{\max}$ is above the plate loading rate V_{pl} but below the seismic threshold. Figure 3f shows the spatiotemporal variation of slip averaged over the depths of the seismogenic zone at each position along the strike. Near the ridge-transform intersections, seismic activity ceases and slip accumulates steadily at the rate of V_{pl}, because of the combined effects of (1) the narrowing seismogenic zone as a result of the half-space cooling thermal structure (Figure 2b), and (2) the bordering fracture zones at the same loading rate V_{pl} and a time-constant slip rate $V = V_{pl}$. This effect continues about 10 km along the strike into the fault on each end, where earthquakes start to break in patches of various sizes. As we will show later, this stabilizing effect is not as pronounced when we utilize the visco-plastic thermal model [*Roland et al.*, 2010]. Among the 19 modeled earthquakes during the 50 year period, the released seismic moment varies greatly. Only 6 events have seismic moment magnitudes large enough ($M_w > 6$) to be visible on Figure 3b. Smaller earthquakes, for example, a M_w = 5.0 and a M_w = 4.5 events at 45.2 and 45.5 yr, respectively, are barely discernible on this figure. It is also clear from Figure 3f that only a very small area of the seismogenic zone has been ruptured during such smaller earthquakes.

[23] Figures 3c and 3d quantify the seismic ($\sum M_{seis}$) to total moment (M_{tot}) ratio within the seismogenic zone, and the slow slip to total moment ratio on the entire transform fault, respectively, as functions of the modeled time period. Our definition of the seismic coupling coefficient χ is equivalent to that by *Boettcher and Jordan* [2004],

$$\chi = \frac{\sum M_{seis}}{M_{tot}} = \frac{\sum M_{seis}}{\mu A_T V_{pl} t} = \frac{\dot{M}_{seis}/(\mu V_{pl})}{A_T} = \frac{A_E}{A_T}, \qquad (7)$$

where $\dot{M}_{seis} \equiv lim_{t\to\infty} \sum M_{seis}/t$ is the OTF moment rate averaged over seismic cycles in a period of t, and effective area is $A_E = \dot{M}_{seis}/(\mu V_{pl})$. As marked in Figure 3c, the coupling coefficient at the end of the simulation (t = 50 year) χ_{final} is taken to be a representative value as the fault has experienced many earthquake cycles. The maximum and minimum values $\chi_{\max}$ and $\chi_{\min}$ are taken as the variation range. The first earthquake in each simulation is not considered in this analysis for results to be free of initial condition effects. After 50 years of slip (~7 m), about 17% of the total moment is released during earthquakes, and about 50% is released in the form of slow slip events, including earthquake nucleation, postseismic relaxation and aseismic transients that are not associated with any earthquakes. We note that increasing the seismic threshold by a factor of 2 would result in slightly smaller moments for all events and a smaller coupling coefficient χ. For example, if V_{seis} = 10 mm/s, χ_{final} = 0.15 ($\chi_{\max}$ = 0.27 and $\chi_{\min}$ = 0.06) and the maximum earthquake moment drops from 5.58 × 10^{18} Nm (M_w = 6.46) to 5.41 × 10^{18} Nm (M_w = 6.45). Such small changes due to the a different "seismic" criterion do not change the modeled earthquake scaling relations, given the large variations in χ for each simulation case.

[24] Figure 4 shows the coseismic slip distributions of the largest earthquakes from simulation runs with W/h^* = 1.16, 1.26, 1.63 (case in Figure 3), and 2.02, using the $a-b$ profile in Figure 2b. The corresponding earthquake moment magnitudes are M_w = 5.6, 6.0, 6.5, and 6.6, respectively. When the seismogenic zone width is about 1.3 times of the earthquake nucleation zone, less than half of the total seismogenic zone area is involved in the largest earthquake rupture. The largest rupture area A_c rapidly increases with W/h^*; at W/h^* = 2.02, A_c nearly occupies the entire seismogenic zone. The relation between A_c and W/h^* will be discussed in more detail in section 3.3. We also note that in the cases of W/h^* = 1.63 and 2.02, the coseismic slip accumulated within the nucleation region is about half of the maximum slip on adjacent fault areas. As will be discussed in section 4, the moderate pre-seismic slip scales with the value of d_c in the seismogenic zone and is consistent with the observation of intense foreshock sequences immediately before the magnitude 6 main shocks on East Pacific Rise transforms [*McGuire et al.*, 2005, 2012].

3.1.2. Visco-plastic Thermal Model

[25] Applying the west Gofar thermal structure calculated from a visco-plastic model as described in Section 2.5 with a Nusselt number N_u = 6 [*Roland et al.*, 2010], we conducted another set of numerical experiments on the short, fast slipping transform (L = 100 km and V_{pl} = 140 mm/yr). The resulting $a-b$ distribution is shown in Figure 2d, and Figure 5 summarizes the results for a case with $W_{\max}/h^*$ = 1.58. Earthquakes occur more frequently and have smaller

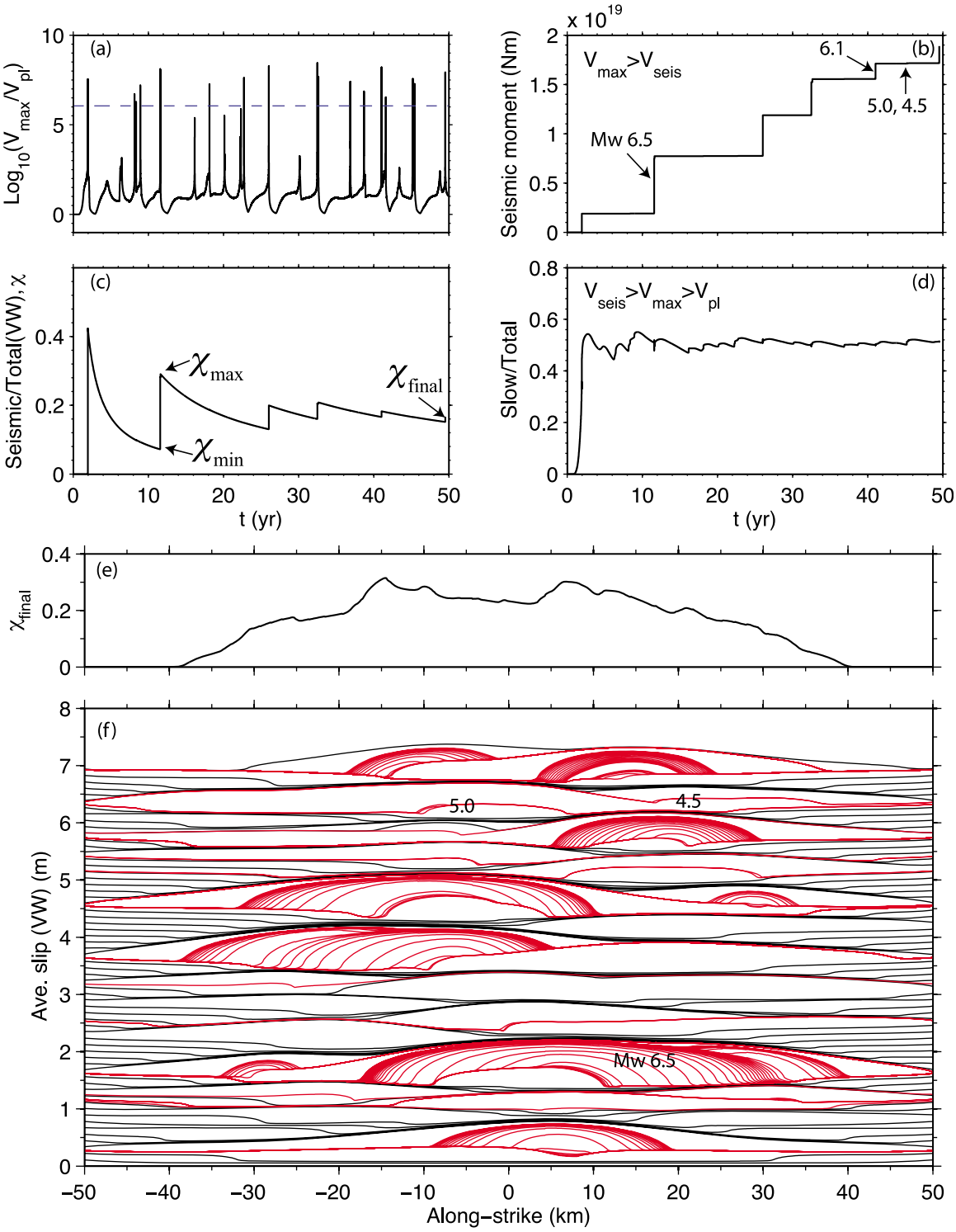

Figure 3. Slip history on a short (L = 100 km) fast-slipping (V_{pl} = 140 mm/yr) transform based on a half-space cooling model with thermal diffusivity κ = 5 mm^2/s. a = 0.015, W/h^* = 1.63. (a) Maximum slip rate $\log_{10}(V_{\max})$ on the fault; (b) cumulative seismic moment, defined when $V_{\max}$ exceeds threshold V_{seis} = 5 mm/s; (c) ratio between seismic moment and total moment within the seismogenic zone; (d) ratio between slow slip moment, defined when $V_{seis} > V_{\max} > V_{pl}$, and total moment released on the entire OTF, as functions of time. Numbers marked on Figure 3b are moment magnitude M_w of selected earthquakes. $\chi_{\max}$, $\chi_{\min}$ and χ_{final} are the maximum, minimum and final values of seismic coupling ratio of the modeled time period after the first earthquake. (e) Final seismic coupling coefficient as a function of along-strike distance on the fault. (f) Average slip accumulated within the seismogenic zone versus distance along strike. Black lines are plotted every 0.8 year to represent interseismic slip. Red lines are plotted every 20 s for coseismic slip.

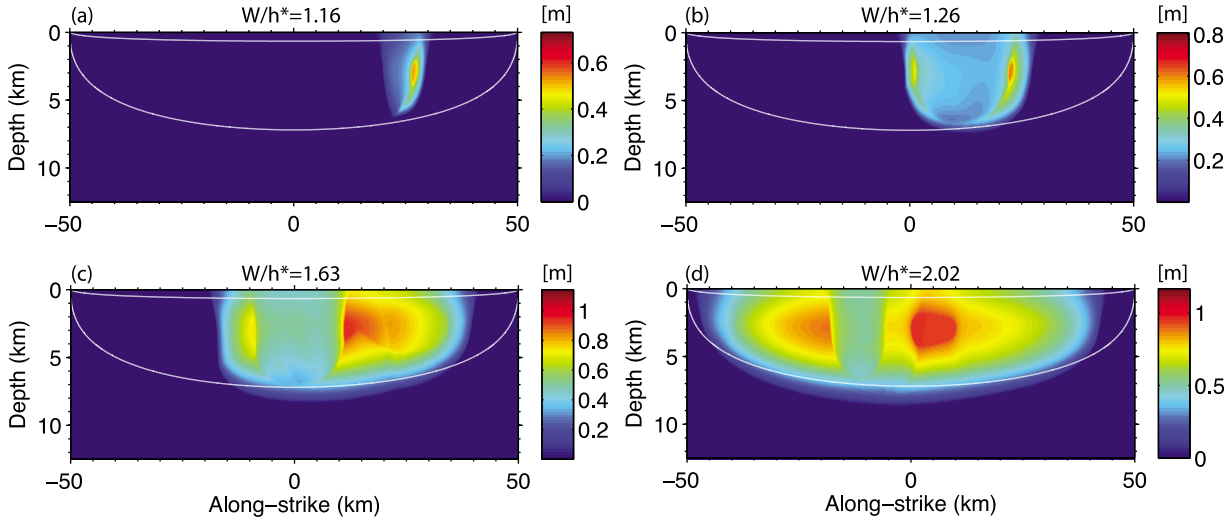

Figure 4. Coseismic slip distribution of the largest earthquake from simulation runs with W/h^* = (a) 1.16, (b) 1.26, (c) 1.63 (Figure 3), and (d) 2.02, for the short, fast-slipping scenario (L = 100 km, V_{pl} = 140 mm/yr) based on the half-space cooling model with κ = 5 mm^2/s. Friction parameter a = 0.015. Corresponding moment magnitudes are M_w = 5.6, 6.0, 6.5 and 6.6, respectively. Area within the white lines is velocity-weakening. Outside region is velocity-strengthening. Note the different color scales for each case.

magnitudes compared to the half-space cooling case; there are 44 earthquakes with the largest magnitude of 5.8 in the modeled 30 year period using the visco-plastic thermal profile, while only 19 earthquakes with a maximum magnitude of 6.5 are predicted in the 50 year period using the half-space cooling model. This difference is attributed to the narrower seismogenic zone and hence smaller seismogenic area predicted by the visco-plastic thermal model (area between white solid lines in Figure 2d). Using a larger Nusselt number deepens the seismogenic zone but does not significantly increase its area. Because of the relative constant seismogenic zone width along the fault, earthquakes can rupture further toward the ridge-transform intersection (RTI) on each side, resulting in a more distributed seismic coupling coefficient along the strike (Figure 5e). This contrasts the predictions from the half-space model in which χ_{final} is largest near the center of the fault and tapers to zero toward the RTIs (Figures 3e and 7e). In total, during the modeled 30 year period, only about 3% of the moment is released during earthquakes, and about 60% is released in the form of aseismic slip.

[26] Figure 6 shows the slip history for the same Gofar-like setup but with a much larger W/h^* = 3.08. Earthquakes of magnitude ~6.3 repeat every 3 years, with each rupture initiating near a RTI, sweeping the entire fault before stopping near the intersection at the other side. Except for the ~10 km zone from the RTI on each side, most part of the fault has a seismic coupling ratio near 1.0, that is, all the moment is released during earthquakes.

3.2. Long, Slow-Slipping Transform Fault

[27] For comparison with the results on short, fast-slipping transforms, we examined a long, slow-slipping scenario with an offset distance L = 500 km and a full spreading rate V_{pl} = 30 mm/yr. This OTF length is chosen as it approaches our computational limit and is the longest case for which visco-plastic thermal model results are available.

[28] For the first set of experiments, we use fault temperatures calculated from the half-space cooling model with a thermal diffusivity κ = 1 mm^2/s. κ is smaller than that in the short, fast-slipping OTF scenario, in order to constrain the seismogenic zone to be less than 20 km in depth, which is approximately the maximum depth of earthquakes on the Romanche transform on the Mid-Atlantic Ridge (L = 920 km). The distribution of $a-b$ is similar in shape to that in Figure 2b. At the center of the fault, the velocity-weakening zone extends from 1.5 km to 15.5 km in depth, corresponding to a maximum seismogenic zone width $W_{\max} \approx$ 14 km. For the case shown in Figure 7, we use d_c = 14 mm and $\bar{\sigma}$ = 50 MPa, resulting in an earthquake nucleation size $h^* \approx$ 8.1 km, hence $W_{\max}/h^* \approx 1.73$. Seismic and slow slip events occur roughly every 20 to 40 years, sometimes with temporally clustered earthquakes, within the modeled 250 year time period. The moment magnitude of the 18 earthquakes ranges from the smallest M_w = 4.2 at t = 86.5 yr, which is almost indiscernible in the cumulative moment (Figure 7b), to the largest M_w = 7.4 at t = 179.3 yr. Even the magnitude 7 ruptures are accompanied by modest aseismic slip released in the form of preseismic nucleation and postseismic relaxation. In total, during the modeled 250 year, about 38% of the moment is released during earthquakes, and about 45% is released in the form of slow slip. A noticeable feature in Figure 7f is that large earthquakes (M_w > 7.0) occur in the central 300 km of the fault, whereas the smaller earthquakes tend to occur closer to the ridge-transform intersections.

[29] For the second set of experiments, we use temperatures calculated from the visco-plastic model with a Nusselt number N_u = 8, which is the upper end of the range of hydrothermal cooling effect investigated by *Roland et al.* [2010]. This high Nusselt number was required to match the presence and depth of magma lens imaged by seismic data over a range of spreading rates [*Phipps Morgan et al.*, 1987]. The model results are qualitatively similar to those for a short, fast-slipping fault, with earthquakes more

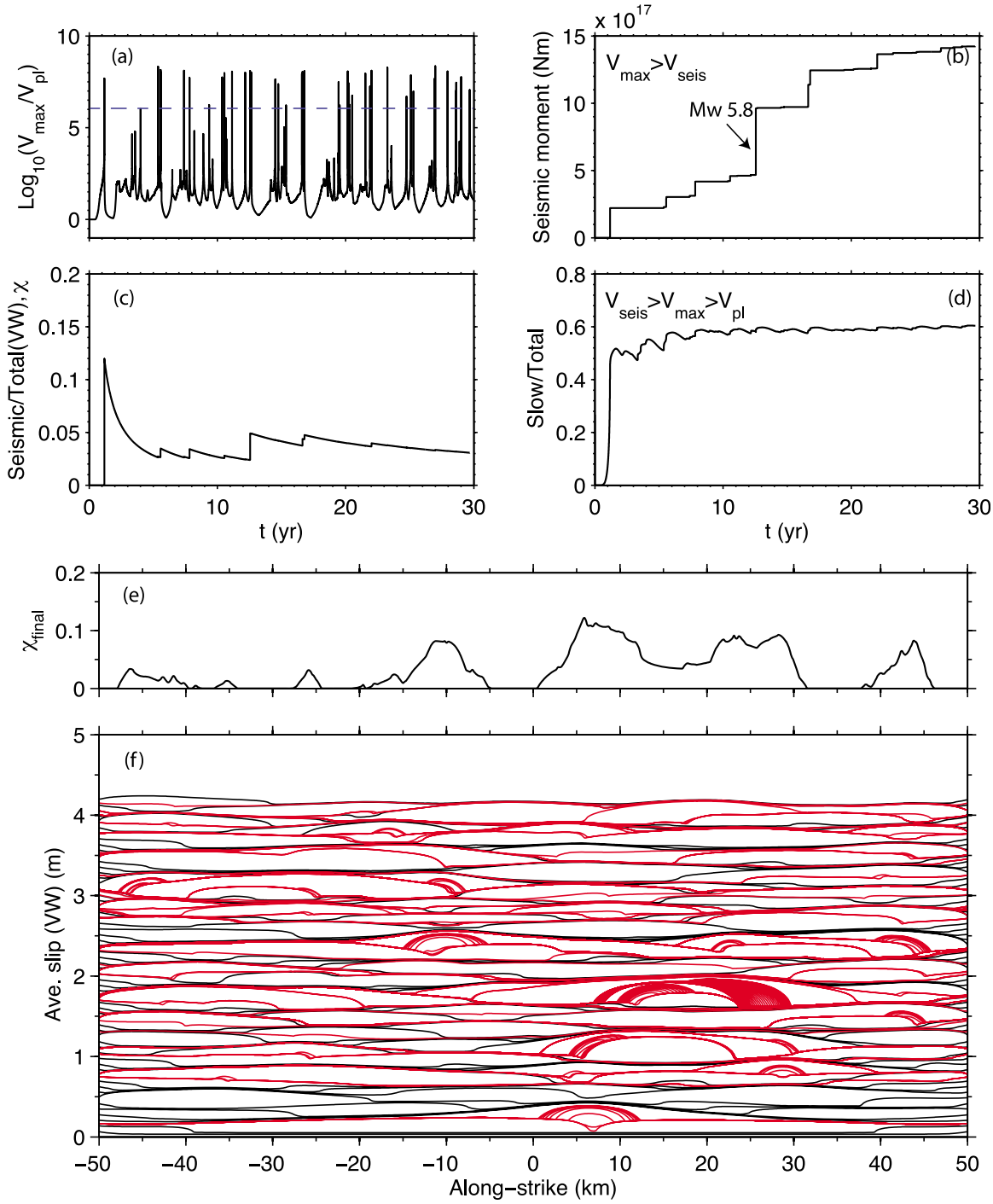

Figure 5. Slip history for a short (L = 100 km) fast-slipping (V_{pl} = 140 mm/yr) transform with fault temperatures calculated from a visco-plastic thermal model for the west Gofar transform [*Roland et al.*, 2010, N_u = 6]. Seismogenic zone is defined between the white solid lines in Figure 2d. Parameter a = 0.015 and W/h^* = 1.58. See Figure 3 caption for symbol descriptions. In Figure 5f black lines are plotted every 0.5 year for interseismic slip. Red lines are plotted every 10 s for coseismic slip.

distributed along the strike and ruptures further toward the RTIs. Modeled earthquakes repeat every 20 to 40 years, with magnitudes in the range of 5 to 7. A detailed discussion on the earthquake magnitude versus its distance to RTI for both sets of simulations will be presented in Section 3.4.

3.3. Modeled Earthquake Scaling Relations

[30] For each scenario discussed above, extensive numerical simulations were conducted to investigate the two characteristic scaling relations summarized from global OTF earthquake catalogs [*Boettcher and Jordan*, 2004]: (1) the low and roughly constant seismic coupling coefficient

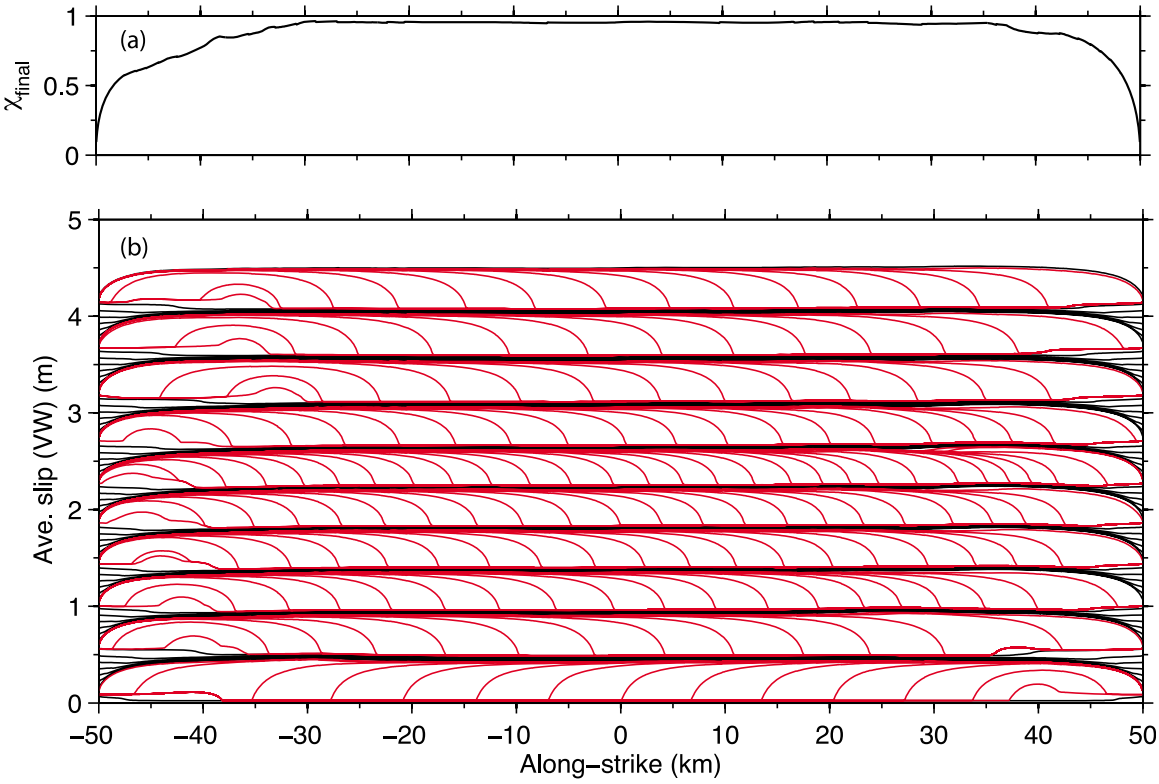

Figure 6. Slip history on a short, fast-slipping OTF using the same parameters as in Figure 5, but with a = 0.01 and W/h^* = 3.08. See Figure 3 caption for symbol descriptions. In Figure 6b black lines are plotted every 0.5 year for interseismic slip. Red lines are plotted every 10 s for coseismic slip.

($\chi = A_E/A_T = 0.15 \pm 0.05$), independent the OTF configuration (L and V_{pl}), and (2) the scaling of the largest earthquake rupture area with the square root of the total seismogenic area ($A_c \propto A_T^{0.5}$). As shown in Figures 3–7, for both the short, fast-slipping and long, slow-slipping OTFs, the ratio of the seismogenic zone width to the earthquake nucleation size (W/h^*) is a key factor in determining χ averaged over many earthquake cycles. To investigate the influence of this ratio on earthquake scaling relations, we conducted a series of calculations in which W/h^* was varied between ~0.9 and 3.5 by changing the characteristic slip distance d_c, hence h^*, within our computational capability.

[31] As shown in Figure 8a, all simulations for different OTF configurations and temperature profiles clearly define a trend of increasing χ with W/h^*, which on the log-linear scale can be broadly divided into three regimes. In Regime I, $W/h^* = 0$ to ~1, the width of the seismogenic zone is too narrow to host any seismic events, so that all slip on the fault occurs aseismically, hence $\chi = 0$. The only exception is a L = 100 km, V_{pl} = 140 mm/yr case with $W/h^* = 0.9$. However, the coupling ratio is so small (less than 0.001) that a slight increase in the "seismic" velocity threshold would result in $\chi = 0$. In Regime II, χ increases by nearly 4 orders of magnitude (10^{-4} to ~1.0) while W/h^* increases from ~1 to 2. It is within this regime, specifically, W/h^* between 1.2 and 1.7, that a roughly constant $\chi = 0.15 \pm 0.05$ is reached. In Regime III where $W/h^* \sim 2$ to $+\infty$, slip on the fault is always released during earthquakes, and thus $\chi \approx 1.0$. Note that for all the OTFs studied by *Boettcher and Jordan* [2004], the actual range of χ varies from as low as 0.01 on the Quebrada transform of the EPR, to as high as 0.53 on the Clipperton transform of the EPR. This is consistent with the range of χ defined in the W/h^* = 1.2–1.7 window. Thus, assuming the thermal and frictional structures discussed above and without introducing further smaller scale along-strike frictional heterogeneities, an OTF seismogenic zone width smaller than twice of the earthquake nucleation size is required for χ to be less than 1.0. Similarly, Figure 8b shows the maximum rupture area A_c, scaled by A_T, increases by 2 orders of magnitude as W/h^* increases from ~1 to 2 within Regime II. For the smallest $W/h^* \sim 0.9$ in which seismic events just start to emerge in the simulations, the largest earthquake only ruptures about 1% of the total seismogenic area. As W/h^* approaches 2 and beyond, the entire A_T is involved in the rupture of the largest earthquake. Indeed, A_c can be greater than A_T as the coseismic rupture propagates slightly into the velocity-strengthening region before termination; such an example is shown in Figures 4c and 4d.

[32] Finally, we examined the relationship between the total seismogenic zone area (A_T), the effective seismic area (A_E) and the maximum rupture area (A_c) for all simulations within the range of W/h^* = 1.2 to 1.7. As expected, A_E increases roughly linearly with A_T and the coupling coefficient χ ranges from ~0.01 to 1, averaging at ~0.1, except for a few L = 500 km cases at the upper bound of W/h^* (Figure 9a). The relation between A_c and A_T is more complicated. When all the simulation cases between W/h^* = 1.2 and 1.7 (within the vertical shaded bar in Figure 8a) are included, $A_c - A_T$ is best fit by a linear relation $A_c \propto A_T$. However, we note in this analysis the coupling coefficient χ

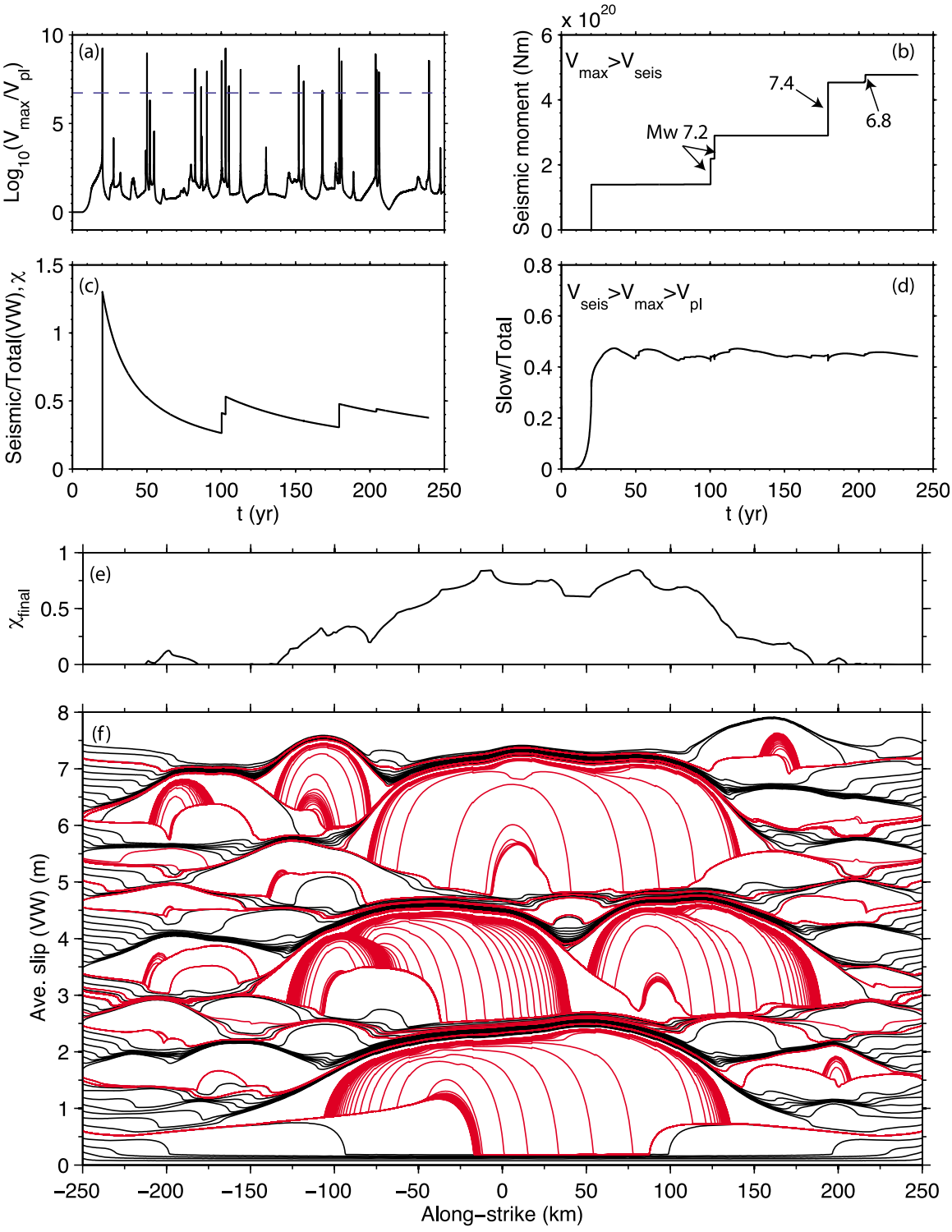

Figure 7. Slip history on a long (L = 500 km) slow-slipping (V_{pl} = 30 mm/yr) transform with a = 0.015, W/h^* = 1.73, based on a half-space cooling model with thermal diffusivity κ = 1 mm^2/s. See Figure 3 caption for symbol descriptions. In Figure 7f black lines are plotted every 4 year to represent interseismic slip. Red lines are plotted every 100 s for coseismic slip. Note the exceptionally long coseismic duration is partly due to the "quasi-dynamic" approximation.

ranges from approximately 0.01 to 1. When only cases with χ between 0.1 and 0.2 are used (i.e., the range of the maximum likelihood values of χ from global observations; the horizontal shaded bar in Figure 8a), $A_c - A_T$ is best described by the relation $A_c \propto A_T^{0.64}$. Both predictions are in general consistence with the observation that the largest OTF earthquakes do not rupture the entire fault. The latter $A_c \propto A_T^{0.64}$ also predicts a deficiency of large earthquakes on long OTFs

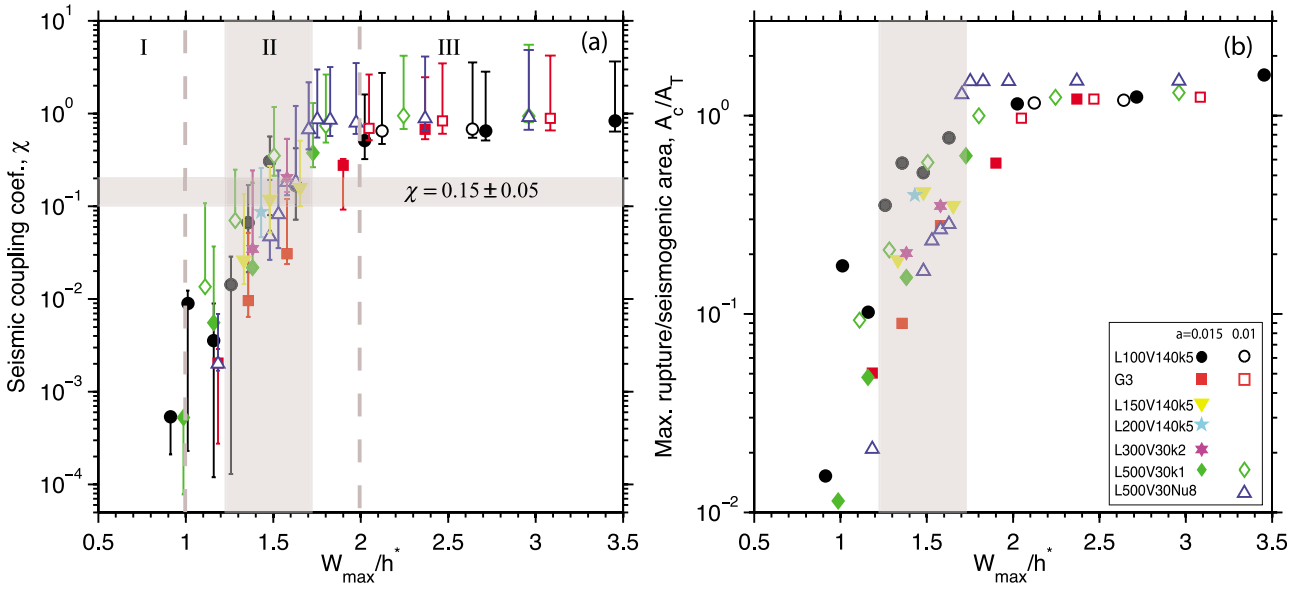

Figure 8. (a) Seismic coupling coefficient χ, and (b) rupture area of the largest earthquake A_c scaled by the seismogenic area A_T, as functions of W_{max}/h^*. Model configurations using the half-space cooling model for fault temperatures include (1) Black: L = 100 km, V_{pl} = 140 mm/yr, κ = 5 mm^2/s, (2) Yellow: L = 150 km, V_{pl} = 140 mm/yr, κ = 5 mm^2/s, (3) Cyan: L = 200 km, V_{pl} = 140 mm/yr, κ = 5 mm^2/s, (4) Magenta: L = 300 km, V_{pl} = 30 mm/yr, κ = 2 mm^2/s, and (5) Green: L = 500 km V_{pl} = 30 mm/yr, κ = 1 mm^2/s. Model configurations using the visco-plastic thermal model are shown in red for west Gofar, EPR, with L = 100 km, V_{pl} = 140 mm/yr and N_u = 6, and in blue for L = 500 km, V_{pl} = 30 mm/yr and N_u = 8. Filled symbols are for friction parameter a = 0.015, and open symbols are for a = 0.01. Error bars represent the maximum and minimum χ as defined in Figure 3c for each simulation. Horizontal shaded bar in Figure 8a marks the global average χ observed by *Boettcher and Jordan* [2004]. Vertical shaded bar is the approximate range in W/h^*, 1.2–1.7, that results in low coupling coefficient close to the observation. The vertical dashed lines approximately divide the diagram into three regimes: (I) W/h^* = 0–1, purely aseismic slip, (II) W/h^* = 1–2, χ increases from $\sim 10^{-4}$ to 1.0, (III) $W/h^* > 2$, full coupled, purely seismic slip.

with large seismogenic zone areas, although it does not exactly reproduce the $A_c \propto A_T^{0.5}$ relation inferred from global OTF earthquakes. One possible reason for this discrepancy is the lack of simulation cases of OTFs longer than 500 km, hence A_T near and greater than 10000 km^2, due to the computational limit in this study. As shown in Figure 1b, the $A_c \propto A_T^{0.5}$ relation is highly dependent on the third and fourth bins of data with A_T greater than 4500 km^2. The longest OTFs studied by *Boettcher and Jordan* [2004] are the Romanche (L = 920 km) and Chile (L = 1120 km) transforms; both with A_T over 20000 km^2. The sparse sample OTF cases in this study (7 different A_T and a total of 18 data points) prevented us from performing a maximum likelihood analysis as by *Boettcher and Jordan* [2004], which may also contribute to the deviation from the observed scaling. In summary, the $A_c - A_T$ relation needs to be further examined in light of more OTF model configurations, particularly longer and larger faults, with sufficient resolution as computer resources expand and visco-plastic thermal model results become available.

3.4. Earthquake Magnitude Versus Distance to the Ridge-Transform Intersection

[33] Based on the regularity of magnitude 6 earthquake occurrences on the Gofar transform fault (the western segment ruptured in 1992, 1997, 2003) [*McGuire*, 2008], an OBS experiment successfully recorded a M_w 6.0 earthquake on September 18, 2008, as well as over 20,000 smaller earthquakes between August 1 and December 30, 2008 [*McGuire et al.*, 2012] (Figure 10a). For events with magnitudes greater than 4.0, Figure 10b shows the moment magnitude as a function of the epicentral distance to the ridge-transform intersection. Here, the RTI distance was calculated by projecting the linear part of the ridge until it reaches the transform fault or the fracture zone. The largest earthquake magnitude decreases with distance to the RTI, with a cluster of 4.0 to 5.0 events extending all the way to the RTI, providing clear evidence for seismogenic behavior close to the RTI.

[34] The magnitude-distance relations of earthquakes modeled on a Gofar-like configuration are shown in Figures 10c and 10d, with $W/h^* \approx 1.6$. When the fault temperatures are calculated from the half-space cooling model, the large earthquakes ($M_w \geq 6.0$) tend to cluster within 10 km of the center of the fault in the along-strike direction. Similar to the trend observed in the data from Gofar, the maximum magnitude decreases as the distance from RTI reduces. However, the seismicity completely ceases at about 20 km from the RTI, suggesting that earthquakes cannot nucleate within the ~20 km of the RTI due to the diminishing width of the seismogenic zone. We note that ruptures of earthquakes nucleated elsewhere on the fault may still propagate for a limited distance into this region, which contributes to a non-zero coupling coefficient to about 10 km from the RTI

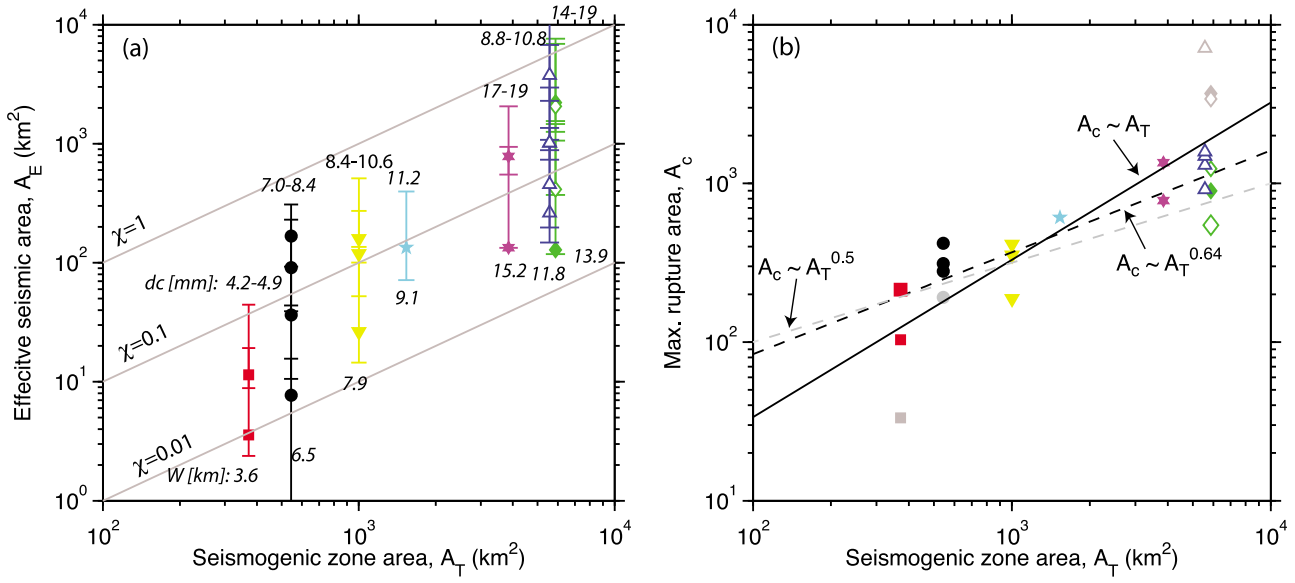

Figure 9. (a) Effective seismic area A_E, and (b) maximum rupture area A_c versus seismogenic zone area A_T, for the simulations shown in Figure 8, with W/h^* between 1.2 and 1.7. Symbols and color coding are the same as in Figure 8. Light grey lines in Figure 9a show the seismic coupling coefficient $\chi = A_E/A_T$ = 0.01, 0.1 and 1.0. Numbers on top of each group of symbols are the values of the characteristic slip distance d_c in mm (or the range, if more than one case), and at the bottom are the values of the maximum seismogenic zone width W in km. In Figure 9b, symbols of regular size as in Figure 9a represent cases within the vertical shaded bar (W/h^* = 1.2–1.7) and are best fit by a linear relation $A_c \propto A_T$ (black solid line); color symbols represent those within the horizontal shaded bar (χ = 0.1–0.2) and are best fit by relation $A_c \propto A_T^{0.64}$ (black dashed line). Grey dashed line shows the observed scaling relations $A_c \propto A_T^{0.5}$.

(Figure 3e). Using the visco-plastic thermal model for western Gofar with N_u = 6, the general relation of a decreasing maximum magnitude with epicentral distance to the RTI still holds, except for two events of magnitude 5.0–5.5 at about 5 km from the RTI. However, unlike the half-space cooling model, earthquakes predicted from the visco-plastic model occur at locations very close to the RTI (the nearest being 2 km in Figure 10d). This results from the nearly uniform width of the seismogenic zone along the strike and suggests that the thermal structure from the visco-plastic model is more realistic for predicting the observed seismicity near the RTI on the Gofar transform.

[35] We also compared the magnitude-distance relation derived for the longest, slow-slipping OTF model (L = 500 km, V_{pl} = 30 mm/yr) to that observed on the Romanche transform (L = 920 km, V_{pl} = 32.5 mm/yr), although their configurations are not identical. As shown in Figure 10e, magnitude 7 earthquakes occur on Romanche with centroids at least ~170 km away from the RTI. Similar to earthquakes on the west Gofar fault, the maximum magnitude here also decreases with the distance to the RTI and seismicity continues to less than 10 km from the RTI. Smaller earthquakes ($M_w \geq 5.5$) populate the entire fault. The model prediction using a half-space cooling thermal structure is similar to the observation in that the maximum magnitude decreases toward the RTI. However, it fails to produce earthquakes very close to the RTI and small events near the center of the fault. By contrast, applying a visco-plastic thermal profile reproduces both features. This further verifies that the visco-plastic thermal model does a better job than the half-space cooling model in predicting earthquake distributions and magnitudes over a range of OTF configurations.

4. Discussion

[36] Without introducing small-scale spatial frictional heterogeneities or temporally evolving stability conditions, our model predicts that when the seismogenic zone width is about 1 to 2 times of the earthquake nucleation zone size (W/h^* = 1 to 2, Regime II in Figure 8) an oceanic transform fault segment can transition between seismic and aseismic slip modes during a time period spanning many earthquake cycles. For example, in the case shown in Figure 3f, the fault segment at x = 10–20 km, which is velocity-weakening above ~7 km in depth, experiences the first earthquake, an aseismic transient event, the largest M_w 6.5 earthquake, six aseismic slip episodes, and two M_w 6.0 earthquakes in the 50 year time sequence. Such alternating behavior between seismic and aseismic slip is likely due to temporal variations in the stress condition on this segment associated with slip occurring on the entire fault. Thus, our model is consistent with the "multimode" hypothesis for OTF behavior, but without requiring temporally evolving friction stability conditions. As W/h^* becomes larger than 2, the seismogenic zone releases moment only in the form of earthquakes.

[37] Besides episodic slow slip events that are not associated with any seismic activity, the large amount of aseismic slip accumulated during the nucleation phase (preseismic slip) also makes a significant contribution to the low seismic coupling coefficient predicted in our models. This effect is

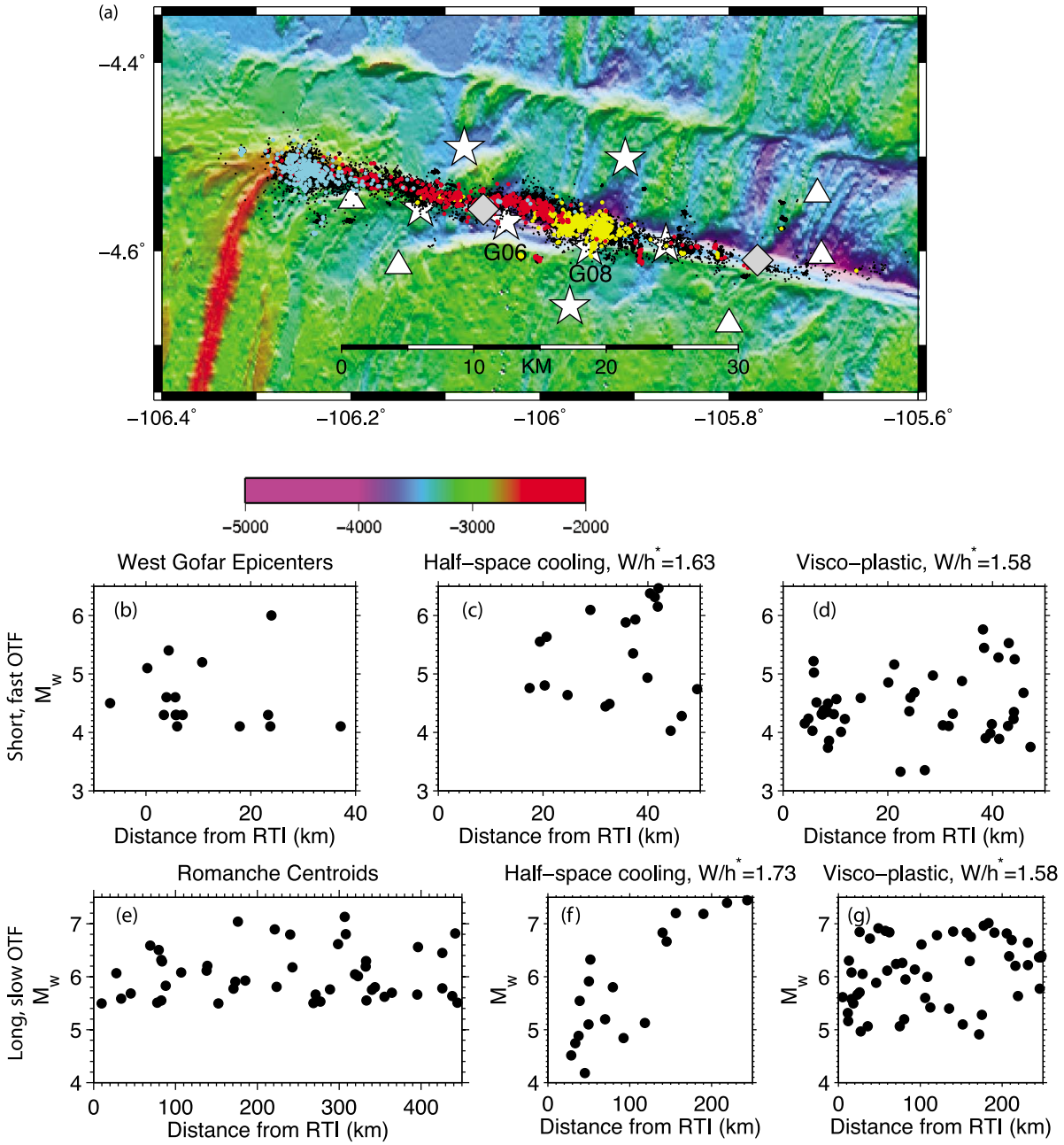

Figure 10. (a) Bathymetric map of the westernmost segment of the Gofar transform fault on the EPR. Background colors denote seafloor depth in meters, white triangles denote broadband seismometers and white stars denote strong motion seismometers. Black dots show the locations of background seismicity from August through December 2008. Foreshocks of the September 18, M_w 6.0 event are shown in yellow. Aftershocks are shown in red, and earthquake swarms in December are shown in cyan [adapted from *McGuire et al.*, 2012]. (b) Distribution of moment magnitude ($M_w \geq 4.0$) of events captured in the 2008 Gofar OBS experiment as a function of their epicentral distances from the ridge-transform-intersection. (c) Modeled earthquake magnitude versus distance from the RTI, for a Gofar-like short, fast spreading OTF (L = 100 km, V_{pl} = 140 mm/yr), with fault temperatures calculated from a half-space cooling model. Friction parameter $a-b$ is shown in Figure 2b, and slip history in Figure 3. (d) Modeled M_w versus RTI distance with temperatures from the west Gofar visco-plastic thermal model with $N_u = 6$. Friction parameter $a-b$ is shown in Figure 2d and slip history in Figure 5. (e) Magnitude versus centroid locations of earthquakes on the Romanche transform (L = 920 km), from GCMT catalog 1976–2011. (f and g) M_w-RTI distance distributions from the longest OTF case in this study, L = 500 km and V_{pl} = 30 mm/yr, using half-space cooling and visco-plastic (N_u = 8) thermal structures, respectively. Note that earthquakes are predicted to occur closer to the RTI with the visco-plastic thermal model, consistent with the observations on Gofar and Romanche transforms.

evident, for example, in the largest earthquake in the short, fast-slipping transform scenario with $W/h^* = 1.63$ and the half-space cooling thermal model (Figure 4c). On the $x = -10$ to 10 km segment, about 0.5 m of preseismic slip accumulates before the maximum slip rate reaches the seismic threshold. About 0.5 m of coseismic slip is released within the nucleation zone as dynamic rupture propagates bilaterally. The maximum coseismic slip is about 1 m at the right edge of the nucleation zone. This relatively large amount of preseismic slip scales with the characteristic slip distance d_c (i.e., smaller d_c would result in smaller preseismic slip), and is consistent with the observation of the intensity of foreshock sequences immediately before main shocks on EPR transform faults. EPR faults are known to have at least an order of magnitude more foreshocks than continental transforms [*McGuire et al.*, 2005]. A swarm of over 20,000 foreshocks ($0 < M_w < 4.5$) preceded the September 18, 2008 Gofar earthquake above the background rate in a 10-km long zone corresponding to a small ($\sim$1 km) geometric step-over [*McGuire et al.*, 2012]. Based on the relative centroid locations of past Gofar magnitude 6 earthquakes, this 10-km long region is inferred to be a barrier to rupture propagation. Furthermore, this area also spatiotemporally coincided with a $\sim$3% average shear wave velocity decrease, suggesting the occurrence of a large aseismic slip event in the foreshock region [*McGuire et al.*, 2012]. In our model, rather than acting as a rupture barrier, the preseismic slip zone initiates dynamic ruptures, which, in most cases, propagate bilaterally along the strike. Thus, it remains to be explored how variations in frictional properties within the nucleation zone, such as changing from gabbro to serpentinite, affect earthquake rupture behavior.

[38] The similar scaling between χ and W/h^* for OTFs with different geometric configurations and thermal structures suggests that the low seismic coupling coefficient observed on global OTFs is not related solely to offset length and/or ridge spreading rate, but to a combination of geometric, thermal and frictional factors. Specifically, in our model, χ is as low as 0.1 on average when W/h^* is within a limited range of 1.2 to 1.7. The importance of W/h^* was also noted in previous numerical studies of the mechanism of episodic slow slip events (SSE), where W was defined as the width of the fault segment under near-lithostatic pore pressure [*Liu and Rice*, 2007; *Rubin*, 2008]. Short-period SSEs, like those observed in natural subduction zones, emerge spontaneously when W/h^* happens to be within a limited range, which varies as different versions of rate and state evolution laws are used. This limited W/h^* range can be relaxed if additional mechanisms that are favorable for slow slip, such as dilatancy, two-state-variable, or cut-off velocity models, are incorporated into the rate and state framework [*Liu and Rice*, 2006; *Shibazaki and Shimamoto*, 2007; *Liu and Rubin*, 2010; *Segall et al.*, 2010]. Such physical mechanisms may also lead to a relaxation of the limited W/h^* range required in our model to explain the low seismic coupling ratio on OTFs. Nevertheless, the present basic model predicts that

$$\frac{W}{h^*} = \frac{\pi W (b-a)^2 \bar{\sigma}}{2\mu^* b d_c} \approx C \tag{8}$$

for the seismic coupling ratio to be roughly 0.15 on OTFs with a wide range of offset lengths and spreading rates. Here, C is a constant between 1.2 and 1.7. As the friction parameters a, b and the effective normal stress $\bar{\sigma}$ are relatively constant for all model cases, the relation in equation (8) reduces to

$$d_c \propto W \propto \sqrt{\kappa L / V_{pl}}. \tag{9}$$

The second part of the relation in equation (9) holds for OTFs with thermal structures calculated from a half-space cooling model. Equation (9) implies that, for OTFs governed by the rate and state frictional properties, the relatively constant low seismic coupling is dictated by a linear relation between the characteristic slip distance d_c and the width of the seismogenic zone W. In particular, longer transform faults associated with slower spreading rates result in wider seismogenic zones extending to greater depths, implying that larger values of d_c are required to achieve the same low χ as on short, fast-slipping transforms.

[39] The possibility of larger d_c at greater depths (or higher normal stress) on longer, slower slipping OTFs is supported by the contact theory of friction [*Bowden and Tabor*, 1950, 1964] and laboratory frictional sliding experiments [*Logan and Teufel*, 1986; *Boettcher et al.*, 2007]. In a microscopic view, the frictional surface is composed of multiple asperities that are in true contact. All such contact areas sum up to the real area of contact A_r, which is generally much smaller than the nominal geometric contact area A. The characteristic slip distance d_c in the rate and state friction law can be interpreted as the critical slip distance necessary to renew surface contacts. Thus d_c is expected to scale with the size of the asperity contacts, or A_r/A. This is supported by olivine rate and state friction experimental data showing a linearly increasing trend of d_c with A_r/A as temperature rises from 600 to 1000°C [*Boettcher et al.*, 2007]. On the other hand, frictional sliding on sandstone and limestone indicates that A_r/A increases approximately linearly with the applied normal stress [*Logan and Teufel*, 1986]. This was interpreted to occur either through an increase in the number of asperity contacts for the elastic sandstone/sandstone interface or via the growth in the size of contacts with normal stress for other plastic properties. Putting these two lines of evidence together, it is plausible that the characteristic slip distance d_c becomes larger at higher normal stresses. Our modeled scaling relation between A_E and A_T suggests that the constant low seismic coupling at OTFs observed globally [*Boettcher and Jordan*, 2004] is the result of a roughly linear relationship between d_c and the depth, hence normal stress, of the seismogenic zone of OTFs at fast to slow spreading centers.

[40] Throughout this study, we have assumed generally homogeneous frictional properties on OTFs. The rate and state friction parameter $a-b$ is taken from a single rock type gabbro, and its spatial distribution is determined by the temperature field on the fault; both the half-space cooling model and the visco-plastic thermal model result in relatively little along-strike variations. There are several aspects of the frictional parameter distribution that need to be improved in future studies.

[41] First, at slower slipping transform faults such as the case presented in Figure 7, the seismogenic zone extends to depths below the oceanic crust and the gabbro friction data used in this study may no longer apply. Hybrid frictional properties such as gabbro in the crust and olivine in the upper mantle seismogenic zone may be more appropriate for OTFs associated with slow spreading ridges.

[42] Second, our current model does not exclude the possibility of an alternate mechanism for generating large percent of aseismic slip on OTFs, namely small-scale along-strike heterogeneities in friction properties. For example, when 15% of the total fault area, in a single patch or multiple patches (each patch is fully coupled), is velocity-weakening (VW) and the rest of the fault is velocity-strengthening (VS), one may also expect the overall seismic coupling coefficient to be around 0.15. Studying earthquake rupture on two VW patches separated by a VS barrier, *Kaneko et al.* [2010] found that the probability for an earthquake to rupture through the VS patch is correlated with the average interseismic coupling on the VS patch. Specifically, they defined a "barrier efficiency" that is proportional to the ratio of the along-strike lengths of the VS and VW patches times $a-b$ (>0) on the VS patch. In the shallow oceanic crust, such VS behavior is possible due to the presence of serpentine as measured in lab experiments [*Reinen et al.*, 1994]. The 10-km segment on western Gofar transform, which is the area of intense foreshock activity and is suggested to have stopped dynamic ruptures from adjacent regions of repeating magnitude 6 earthquakes [*McGuire*, 2008; *McGuire et al.*, 2012], may be a representation of such a VS aseismic barrier.

[43] Third, in our model the size of the smallest earthquakes is constrained by the nucleation size h^*, which is on the order of 4 km in the Gofar-like models. Consequently, the smallest modeled earthquakes are of magnitude 3.5 to 4.0. Thus, with the generally homogeneous frictional property distribution assumed in this study, we cannot reproduce the abundant magnitude 0 to 1 events observed on global OTFs. Small VW patches on the scale of 10s of meters embedded in a large VS region may be needed in order to generate such small events as well as large ones that follow the scaling relations.

[44] Finally, finer details observed during OTF earthquake rupture processes, such as the migration of earthquake swarms and inferred low stress drop on Gofar [*Roland and Mcguire*, 2009], shear wave velocity increase prior to the 2008 M6 Gofar event and multiple episodes of velocity drop during swarm activity [*McGuire et al.*, 2012], should provide useful constraints to the construction of various degrees of heterogeneities in future OTF model studies.

5. Conclusion

[45] In this study, we have investigated earthquake behavior and scaling relations on oceanic transform faults using a 3-D model incorporating the "ageing" version of the rate- and state-dependent friction with a single state variable. The frictional parameter $a-b$ is adapted from experimental measurements on gabbro gouge under hydrothermal conditions, and mapped to OTFs using temperatures calculated from (1) a half-space cooling model and (2) a thermal model that takes into account physical processes such as the visco-plastic rheology of the lithosphere, non-Newtonian temperature-dependent viscous flow in the underlying mantle, and the effects of shear heating and hydrothermal circulation. For a wide range of fault lengths, full spreading rates and thermal structures, we simulated slip history and constructed earthquake catalogs over many earthquake cycles. The seismic coupling coefficient χ was calculated as the ratio of the seismic moment released by all earthquakes to the total moment accumulated by plate loading in the seismogenic zone during the simulated time period [*Boettcher and Jordan*, 2004].

[46] All simulation cases show that the degree of seismic coupling χ is controlled by W/h^*, the ratio of the seismogenic zone width (where $a - b < 0$) and the earthquake nucleation size, which is in turn related to friction parameters a, b, d_c, and the effective normal stress $\bar{\sigma}$. We found that χ increases by about 4 orders of magnitude, from 10^{-4} to 1, within a limited range of W/h^* from ~1 to 2. Slip is released aseismically when $W/h^* < 1$ and entirely in earthquakes for $W/h^* > 2$. This trend is observed in all modeled OTFs, ranging from short, fast-slipping (L = 100 km and V_{pl} = 140 mm/yr, Gofar-like, East Pacific Rise) to long, slow-slipping (L = 500 km and V_{pl} = 30 mm/yr, Doldrums-like, Mid-Atlantic Ridge) transform faults and regardless of the thermal model used. Similarly, the area ruptured by the largest earthquake (A_c) in the modeled catalog increases dramatically with W/h^*. Only about 1% of the total seismogenic zone area (A_T) is ruptured during the largest event at $W/h^* \sim 0.9$, while the entire A_T is ruptured when $W/h^* > 2$. An average seismic coupling of $\chi = 0.15 \pm 0.05$ is reached at $W/h^* \approx 1.2$–1.7. The resulting linear increase of the effective seismic area (A_E) with A_T can be explained by an increase in the characteristic slip distance d_c on longer and slower slipping OTFs, where the seismogenic zone is wider and normal stresses are higher. For cases within $W/h^* \approx 1.2$–1.7, the largest earthquake rupture area A_c is less than the seismogenic area A_T. In particular, when only cases with χ between 0.1 and 0.2 (the range inferred from global observations) are considered, the relation is best described by $A_c \propto A_T^{0.64}$, which is consistent with the observed deficiency of large earthquakes on long, slow-slipping faults. Its deviation from the observed $A_c \propto A_T^{0.5}$ is possibly a result of the lack of large fault cases ($A_T > 10000$ km^2) in the present study due to computational constraint.

[47] In summary, our modeling results provide an explanation for the globally observed low seismic coupling and deficiency of large earthquakes on oceanic transform faults without the need to invoke small-scale heterogeneous frictional properties, assuming that the seismogenic zone is roughly 1.2 to 1.7 of the size of the earthquake nucleation zone. Future work should investigate how spatially and/or temporally heterogeneous friction properties may affect the OTF earthquake source characteristics and scaling relations, with a focus on the Quebrada, Discovery and Gofar transform system on the East Pacific Rise, where abundant ocean bottom seismometer data are available to constrain the friction heterogeneities.

[48] **Acknowledgments.** We thank Emily Roland for providing her visco-plastic thermal model results, and Greg Hirth for discussion on rock frictional sliding experiments. We thank two anonymous reviewers and the Associate Editor for their comments that helped to improve the presentation

of this paper. This work was supported by NSF-EAR award 1015221, NSF-OCE award 1061203, and a J. Lamar Worzel Assistant Scientist Fund to Y. Liu at WHOI.

References

Abercrombie, R., and G. Ekström (2001), Earthquake slip on oceanic transform faults, *Nature*, *410*(6824), 74–77.

Beeler, N. M., T. E. Tullis, and J. D. Weeks (1994), The roles of time and displacement in the evolution effect in rock friction, *Geophys. Res. Lett.*, *21*(18), 1987–1990.

Behn, M., J. Lin, and M. T. Zuber (2002), Evidence for weak oceanic transform faults, *Geophys. Res. Lett.*, *29*(24), 2207, doi:10.1029/2002GL015612.

Behn, M., M. Boettcher, and G. Hirth (2007), On the thermal structure of oceanic transform faults, *Geology*, *35*(4), 307–310.

Bird, P., Y. Kagan, and D. Jackson (2002), Plate tectonics and earthquake potential of spreading ridges and oceanic transform faults, in *Plate Boundary Zones*, *Geodyn. Ser.*, vol. 30, edited by S. Stein and J. T. Freymueller, pp. 203–218, AGU, Washington, D. C.

Blanpied, M. L., C. J. Marone, D. A. Lockner, J. D. Byerlee, and D. P. King (1998), Quantitative measure of the variation in fault rheology due to fluid-rock interactions, *J. Geophys. Res.*, *103*(B5), 9691–9712.

Boettcher, M. S., and T. H. Jordan (2004), Earthquake scaling relations for mid-ocean ridge transform faults, *J. Geophys. Res.*, *109*, B12302, doi:10.1029/2004JB003110.

Boettcher, M., and J. McGuire (2009), Scaling relations for seismic cycles on mid-ocean ridge transform faults, *Geophys. Res. Lett.*, *36*, L21301, doi:10.1029/2009GL040115.

Boettcher, M. S., G. Hirth, and B. Evans (2007), Olivine friction at the base of oceanic seismogenic zones, *J. Geophys. Res.*, *112*, B01205, doi:10.1029/2006JB004301.

Bohnenstiehl, D., M. Tolstoy, R. Dziak, C. Fox, and D. Smith (2002), Aftershock sequences in the mid-ocean ridge environment: An analysis using hydroacoustic data, *Tectonophysics*, *354*(1–2), 49–70.

Bowden, F. P., and D. Tabor (1950), *The Friction and Lubrication of Solids, Part I*, Clarenden, Oxford, U. K.

Bowden, F. P., and D. Tabor (1964), *The Friction and Lubrication of Solids, Part II*, Clarenden, Oxford, U. K.

Braunmiller, J., and J. Nábělek (2008), Segmentation of the Blanco Transform Fault Zone from earthquake analysis: Complex tectonics of an oceanic transform fault, *J. Geophys. Res.*, *113*, B07108, doi:10.1029/2007JB005213.

Cannat, M., et al. (1995), Thin crust, ultramafic exposures, and rugged faulting patterns at the Mid-Atlantic Ridge (22–24 N), *Geology*, *23*(1), 49–52.

Chen, T., and N. Lapusta (2009), Scaling of small repeating earthquakes explained by interaction of seismic and aseismic slip in a rate and state fault model, *J. Geophys. Res.*, *114*, B01311, doi:10.1029/2008JB005749.

Dieterich, J. H. (1979), Modeling of rock friction: 1. Experimental results and constitutive equations, *J. Geophys. Res*, *84*(B5), 2161–2168.

Engeln, J., D. Wiens, and S. Stein (1986), Mechanisms and depths of Atlantic transform earthquakes, *J. Geophys. Res.*, *91*, 548–577.

He, C., Z. Wang, and W. Yao (2007), Frictional sliding of gabbro gouge under hydrothermal conditions, *Tectonophysics*, *445*, 353–362, doi:10.1016/j.tecto.2007.09.008.

Kagan, Y., P. Bird, and D. Jackson (2010), Earthquake forecasting in diverse tectonic zones of the globe, *Pure Appl. Geophys.*, *167*, 1–21.

Kaneko, Y., J. Avouac, and N. Lapusta (2010), Towards inferring earthquake patterns from geodetic observations of interseismic coupling, *Nat. Geosci.*, *3*, 363–369, doi:10.1038/NGEO0843.

Lapusta, N., and Y. Liu (2009), Three-dimensional boundary integral modeling of spontaneous earthquake sequences and aseismic slip, *J. Geophys. Res.*, *114*, B09303, doi:10.1029/2008JB005934.

Lapusta, N., and J. R. Rice (2003), Nucleation and early seismic propagation of small and large events in a crustal earthquake model, *J. Geophys. Res.*, *108*(B4), 2205, doi:10.1029/2001JB000793.

Lapusta, N., J. R. Rice, Y. Ben-Zion, and G. Zheng (2000), Elastodynamic analysis for slow tectonic loading with spontaneous rupture episodes on faults with rate- and state-dependent friction, *J. Geophys. Res.*, *105*(B10), 23,765–23,789.

Liu, Y., and J. R. Rice (2005), Aseismic slip transients emerge spontaneously in three-dimensional rate and state modeling of subduction earthquake sequences, *J. Geophys. Res.*, *110*, B08307, doi:10.1029/2004JB003424.

Liu, Y., and J. R. Rice (2006), Recurrence interval and magnitude of aseismic deformation transients: An investigation using rate- and state-dependent friction, *Eos Trans. AGU*, *87*(52), Fall Meet. Suppl., Abstract T41A-1543.

Liu, Y., and J. R. Rice (2007), Spontaneous and triggered aseismic deformation transients in a subduction fault model, *J. Geophys. Res.*, *112*, B09404, doi:10.1029/2007JB004930.

Liu, Y., and J. R. Rice (2009), Slow slip predictions based on granite and gabbro friction data compared to GPS measurements in northern Cascadia, *J. Geophys. Res.*, *114*, B09407, doi:10.1029/2008JB006142.

Liu, Y., and A. M. Rubin (2010), Role of fault gouge dilatancy on aseismic deformation transients, *J. Geophys. Res.*, *115*, B10414, doi:10.1029/2010JB007522.

Logan, J., and L. Teufel (1986), The effect of normal stress on the real area of contact during frictional sliding in rocks, *Pure Appl. Geophys.*, *124*, 471–486.

McGuire, J. (2008), Seismic cycles and earthquake predictability on East Pacific Rise transform faults, *Bull. Seismol. Soc. Am.*, *98*(3), 1067–1084.

McGuire, J., M. Boettcher, and T. Jordan (2005), Foreshock sequences and short-term earthquake predictability on East Pacific Rise transform faults, *Nature*, *434*(7032), 457–461.

McGuire, J., J. A. Collins, P. Gouedard, E. Roland, D. Lizarralde, M. S. Boettcher, M. D. Behn, and R. D. van der Hilst (2012), Capturing the end of a seismic cycle on the Gofar transform fault, East Pacific Rise, *Nat. Geosci.*, in press.

McKenzie, D. P. (1969), Speculations on the consequences and causes of plate motions, *Geophys. J. R. Astron. Soc.*, *18*, 1–32.

Okada, Y. (1992), Internal deformation due to shear and tensile faults in a half-space, *Bull. Seismol. Soc. Am.*, *82*(2), 1018–1040.

Phipps Morgan, J., E. Parmentier, and J. Lin (1987), Mechanisms for the origin of mid-ocean ridge axial topography: Implications for the thermal and mechanical structure of accreting plate boundaries, *J. Geophys. Res.*, *92*, 12,823–12,836.

Reinen, L. A. (2000a), Slip styles in a spring-slider model with a laboratory-derived constitutive law for serpentinite, *Geophys. Res. Lett.*, *27*(14), 2037–2040.

Reinen, L. A. (2000b), Seismic and aseismic slip indicators in serpentinite gouge, *Geology*, *28*(2), 135–138.

Reinen, L. A., J. D. Weeks, and T. E. Tullis (1994), The frictional behavior of lizardite and antigorite serpentinites: Experiments, constitutive models, and implications for natural faults, *Pure. Appl. Geophys.*, *143*(1–3), 317–358.

Rice, J. R. (1992), Fault stress states, pore pressure distributions, and the weakness of the San Andreas Fault, in *Fault Mechanics and Transport Properties*, edited by B. Evans and T.-F. Wong, pp. 475–503, Elsevier, New York.

Rice, J. R. (1993), Spatiotemporal complexity of slip on a fault, *J. Geophys. Res.*, *98*(B6), 9885–9907.

Rice, J. R., and Y. Ben-Zion (1996), Slip complexity in earthquake fault models, *Proc. Natl. Acad. Sci. U. S. A.*, *93*(9), 3811–3818.

Rice, J. R., and A. L. Ruina (1983), Stability of steady frictional slipping, *J. Appl. Mech.*, *50*(2), 343–349.

Rice, J. R., N. Lapusta, and K. Ranjith (2001), Rate and state dependent friction and the stability of sliding between elastically deformable solids, *J. Mech. Phys. Solids*, *49*, 1865–1898.

Roland, E., and J. J. Mcguire (2009), Earthquake swarms on transform faults, *Geophys. J. Int.*, *178*, 1677–1690, doi:10.1111/j.1365-246X.2009.04214.x.

Roland, E., M. Behn, and G. Hirth (2010), Thermal-mechanical behavior of oceanic transform faults: Implications for the spatial distribution of seismicity, *Geochem. Geophys. Geosyst.*, *11*, Q07001, doi:10.1029/2010GC003034.

Rubin, A. M. (2008), Episodic slow slip events and rate-and-state friction, *J. Geophys. Res.*, *113*, B11414, doi:10.1029/2008JB005642.

Rubin, A. M., and J.-P. Ampuero (2005), Earthquake nucleation on (agine) rate and state faults, *J. Geophys. Res.*, *110*, B11312, doi:10.1029/2005JB003686.

Ruina, A. L. (1983), Slip instability and state variable friction laws, *J. Geophys. Res.*, *88*(B12), 10,359–10,370.

Segall, P., A. M. Rubin, M. Bradley, and J. R. Rice (2010), Dilatant strengthening as a mechanism for slow slip events, *J. Geophys. Res.*, *115*, B12305, doi:10.1029/2010JB007449.

Shibazaki, B., and T. Shimamoto (2007), Modelling of short-interval silent slip events in deeper subduction interfaces considering the frictional properties at the unstable-stable transition regime, *Geophys. J. Int.*, *171*(1), 191–205, doi:10.1111/j.1365-246X.2007.03434.x.

Sleep, N. (1975), Formation of oceanic crust: some thermal constraints, *J. Geophys. Res.*, *80*, 4037–4042.

Sykes, L. R., and G. Ekström (2012), Earthquakes along Eltanin transform system, SE Pacific Ocean: Fault segments characterized by strong

and poor seismic coupling and implications for long-term earthquake prediction, *Geophys. J. Int.*, *188*(2), 421–434, doi:10.1111/j.1365-246X.2011.05284.x.

Tucholke, B., and J. Lin (1994), A geological model for the structure of ridge segments in slow spreading ocean crust, *J. Geophys. Res.*, *99*(B6), 11,937–11,958.

Wilcock, W., G. Purdy, and S. Solomon (1990), Microearthquake evidence for extension across the Kane Transform Fault, *J. Geophys. Res.*, *88*, 6455–6468.

M. D. Behn and J. J. McGuire, Department of Geology and Geophysics, Woods Hole Oceanographic Institution, Woods Hole, MA 02543, USA. (mbehn@whoi.edu; jmcguire@whoi.edu)

Y. Liu, Department of Earth and Planetary Sciences, McGill University, Montreal, QC H3A 2A7, Canada. (yajing.liu@mcgill.ca)